REPORT DOCUMENTATION PAGE

Form Approved
OMB No. 0704-0188

1. REPORT DATE (DD-MM-YYYY) 08/14/07	2. REPORT DATE Final	3. DATES COVERED (From - To) 2-1-04 to 3-31-07

4. TITLE AND SUBTITLE	5a. CONTRACT NUMBER
High Fidelity Multidisciplinary Design using an Integrated Design Environment	
	5b. GRANT NUMBER FA9550-04-1-0051
	5c. PROGRAM ELEMENT NUMBER

6. AUTHOR(S)	5d. PROJECT NUMBER
Antony Jameson	
	5e. TASK NUMBER
	5f. WORK UNIT NUMBER

7. PERFORMING ORGANIZATION NAME(S) AND ADDRESS(ES)	8. PERFORMING ORGANIZATION REPORT NUMBER
Stanford University, Stanford, Ca 94305. MC :4035	

9. SPONSORING/MONITORING AGENCY NAME(S) AND ADDRESS(ES)	10. SPONSOR/MONITOR'S ACRONYM(S)
Air Force Office of Scientific Research 875 North Randolf Street, Room 3112 Arlington, VA 22203	AFOSR
Dr Fariba Fahroo	11. MONITORING AFRL-SR-AR-TR-07-0357

12. DISTRIBUTION AVAILABILITY STATEMENT

Public
Approved for public release. Distribution is unlimited

13. SUPPLEMENTARY NOTES

14. ABSTRACT

The main objectives of the research was to further develop the necessary fundamental algorithms to enable high fidelity multi-disciplinary design of complete aircraft configurations. The work was focused on four main areas: (1) Flow solution algorithms for unstructured meshes, (2) Aero-structural plan-form optimization (3) Multi-fidelity approach to multi-disciplinary design of supersonic aircraft. (4) Algorithms for automatic feedback control of aerodynamic flows.

15. SUBJECT TERMS

Computational Algorithms; Multidisciplinary Design; Optimization; Control of Aerodynamic Flows

16. SECURITY CLASSIFICATION OF:			17. LIMITATION OF ABSTRACT	18. NUMBER OF PAGES	19a. NAME OF RESPONSIBLE PERSON
a. REPORT	b. ABSTRACT	c. THIS PAGE			Antony Jameson
U	U	U	UU	38	19b. TELEPONE NUMBER (Include area code) 650-723-2867 (Carolyn Edwards)

Standard Form 298 (Rev. 8-98)
Prescribed by ANSI-Std Z39-18

High-Fidelity Multidisciplinary Design Using an Integrated Design Environment

AFOSR GRANT NO. AF FA 9550-04-1-0051

FINAL REPORT (March 2004–February 2007)

Antony Jameson
Department of Aeronautics & Astronautics
Stanford University
Stanford, CA 94305

Executive Summary

Building on our previous work, the main objectives of this research were to further develop and expand the necessary fundamental algorithms and procedures to enable high-fidelity multidisciplinary design of complete aircraft configurations. Based on a number of achievements in our previous work, we believe that we have a mathematical formulation for the tools that are required to create such an integrated design environment. We were able to increase the scope of our research by leveraging from other sources of support. In particular Georg May's thesis work benefited from the support of a Stanford Graduate Fellowship.

In order to realize a truly automated multidisciplinary design environment, several tasks needed to be accomplished to enhance the tools that we already had and to integrate them in such a way that coordination between the evolution of the disciplines is maintained.

This report describes the progress that has been made towards the accomplishment of these goals. The fundamental efforts conducted have focused on four different areas. Firstly, we have continued to develop our analysis and design unstructured mesh capabilities for viscous flows; a later section provides a summary of this work. Secondly, we have further developed our viscous planform optimization capability which now includes a model of the wing weight to guide the selection of the planform variables (area, aspect ratio, sweep, taper ratio, etc.). Third, we have carried out initial efforts to create truly high-fidelity multidisciplinary designs by creating a two-level, multi-fidelity design strategy that has been demonstrated using a small supersonic jet as an example. Finally, we have explored the possibility of developing automcatic feedback control of aerodynamic flows based on a combination of adjoint based sensitivity analysis, reduced order modelling, and linear quadratic control theory. A procedure for controlling the surface pressure disturbances via blowing and suction has been demonstrated and this has been extended to show the possibility of active flutter control.

The theses and main publications which have resulted from the research performed in association with the grant are listed below.

20070925277

1

Theses under AFOSR 9550-04-1-0051
March 2004–February 2007

1. Kasidit Leoviriyakit, "Wing Planform Optimization via an Adjoint Method", Ph.D. Dissertation, Stanford University, March 2005.

2. Seongim Choi, "Multi-Fidelity Multi-Disciplinary Design Optimization of Supersonic Business Jets", Ph.D. Dissertation, Stanford University, December 2005.

3. Georg May, "A Kinetic Scheme for the Navier-Stokes Equations and High-Order Methods for Hyperbolic Conservation Laws", Ph.D. Dissertation, Stanford University, September 2006.

4. Karthik Palaniappan, "Algorithms for Automatic Feedback Control of Aerodynamic Flows", Ph.D. Dissertation, Stanford University, June 2007.

Publications under AFOSR 9550-04-1-0051
March 2004–February 2007

1. A. Jameson, "Advances in Aerodynamic Shape Optimization", International Conference on Computational Fluid Dynamics (ICCFD3), Toronto, Canada, July 12-16 2004.

2. K. Palaniappan and A. Jameson, "An Analysis of Bodies Having Minimum Pressure Drag in Supersonic Flow: Exploring the Nonlinear Domain", International Conference on Computational Fluid Dynamics (ICCFD3), Toronto, Canada, July 12-16 2004.

3. K. Leoviriyakit and A. Jameson, "Case Studies in Aero-Structural Wing Planform and Section Optimization", 22nd AIAA Applied Aerodynamics Conference and Exhibit, AIAA Paper 2004-5372, RI, August 16-19, 2004.

4. K. Palaniappan and A. Jameson, "Bodies Having Minimum Pressure Drag in Supersonic Flow: Investigating Nonlinear Effects", 22nd AIAA Applied Aerodynamics Conference and Exhibit, AIAA Paper 2004-5383, RI, August 16-19, 2004.

5. P. LeGresley and J. Alonso, "Improving the Performance of Design Decomposition Methods with POD", 10th AIAA/ISSMO Multidisciplany Analysis and Optimization Conference, AIAA Paper 2004-4465, Albany, NY, August 30-September 1, 2004.

6. J. Alonso, P. LeGresley, E. van der Weide and J. Martins, J, "pyMDO: A Framework for High-Fidelity Multi-Disciplinary Optimization", 10th AIAA/ISSMO Multidisciplany Analysis and Optimization Conference, AIAA Paper 2004-4480, Albany, NY, August 2004.

7. K. Leoviriyakit, S. Kim and A. Jameson, "Aero-Structural Wing Planform Optimization Using the Navier-Stokes Equations", 10th AIAA/ISSMO Multidisciplany Analysis and Optimization Conference, AIAA Paper 2004-4479, Albany, NY, August 30-September 1, 2004.

8. A. Jameson, "Efficient Aerodynamic Shape Optimization", 10th AIAA/ISSMO Multidisciplany Analysis and Optimization Conference, AIAA Paper 2004-4369, Albany, NY, August 30-September 1, 2004.

9. S. Choi, J. Alonso, I. Kroo and M. Wintzer, "Multi-Fidelity Design Optimization of Low-Boom Supersonic Business Jets", 10th AIAA/ISSMO Multidisciplinary Analysis and Optimization Conference, AIAA Paper 2004-4371, Albany, NY, September 2004 (Invited to the 1st International Conference on Flow Dynamics, Nov., Sendai, Japan).

10. Aerodynamics. In: Encyclopedia of Computational Mechanics (Vol 3, Chapter 11). E. Stein, R. De Borst, and T.J.R. Hughes (Eds.), Wiley 2004.

11. G. May, B. Srinivasan and A. Jameson, "Calculating Three-Dimensional Transonic Flow using a Gas-Kinetic BGK Finite-Volume Method", 43rd AIAA Aerospace Sciences Meeting & Exhibit, AIAA Paper 2005-1397, Reno, NV, January 10-13, 2005.

12. M. Harbeck and A. Jameson, "Exploring the Limits of Transonic Shock-free Airfoil Design", 43rd AIAA Aerospace Sciences Meeting & Exhibit, AIAA Paper 2005-1041, Reno, NV, January 10-13, 2005.

13. K. Leoviriyakit and A. Jameson, "Multi-point Wing Planform Optimization via Control Theory", 43rd AIAA Aerospace Sciences Meeting & Exhibit, AIAA Paper 2005-0450, Reno, NV, January 10-13, 2005.

14. A. Jameson, Sriram, L. Martinelli, S. Sliff and S. Thomas, "Aerodynamic Shape Optimization of Transonic and Supersonic Aircraft Configurations", 43rd AIAA Aerospace Sciences Meeting & Exhibit, AIAA Paper 2005-1013, Reno, NV, January 10-13, 2005.

15. S. Choi, J. Alonso, S. Kim, I. Kroo and M. Wintzer, "Two-Level Multi-Fidelity Design Optimization Studies for Supersonic Jets", 43rd AIAA Aerospace Sciences Meeting & Exhibit, AIAA Paper 2005-0531, Reno, NV, January 10-13, 2005.

16. G. May and A. Jameson, "High-Order Accurate Methods for High-Speed Flow", AIAA Paper 2005-5252 , 17th AIAA Computational Fluid Dynamics Conference, Toronto, Ontario, Canada, June 6-9, 2005.

17. S. Choi, J. Alonso and I. Kroo, "Multi-Fidelity Design Optimization Studies for Supersonic Jets Using Surrogate Management Frame Method", 23rd AIAA Applied Aerodynamics Conference, AIAA Paper 2005-5007, Toronto, Ontario, Canada, June 2005.

18. J. Alonso, S. Choi, E. van der Weide, "Global and Local Multi-Disciplinary Techniques for Supersonic Jet Design", 23rd AIAA Applied Aerodynamics Conference, AIAA Paper 2005-4798, Toronto, Ontario, Canada, June 2005.

19. G. May and A. Jameson, "Improved Gaskinetic Multigrid Method for Three-Dimensional Computation of Viscous Flow", 17th AIAA Computational Fluid Dynamics Conference, AIAA Paper 2005-5106, Toronto, Ontario, June 6-9, 2005.

20. G. May and A. Jameson, "A Spectral Difference Method for the Euler and Navier-Stokes Equations on Unstructured Meshes", 44th AIAA Aerospace Sciences Meeting & Exhibit, AIAA Paper 2006-0449, Reno, NV, January 9-12, 2006.

21. A. Jameson, R. Hu, B. Kerchenfaut, D. Griswold and K. Leoviriyakit, "Aerodynamic Shape Optimization for the World's Fastest P-51", 44th AIAA Aerospace Sciences Meeting & Exhibit, AIAA Paper 2006-0449, Reno, NV, January 9-12, 2006.

22. K. Panaliappan, P. Sahu, J. Alonso and A. Jameson, "Active Flutter Control using an Adjoint Method", 44th AIAA Aerospace Sciences Meeting & Exhibit, AIAA Paper 2006-844, Reno, NV, January 9-12, 2006.

23. K. Palaniappan and A. Jameson, "Feedback Control of Aerodynamic Flows", 44th AIAA Aerospace Sciences Meeting & Exhibit, AIAA Paper 2006-843, Reno, NV, January 9-12, 2006.

24. J. Vassberg and A. Jameson, "Aerodynamic Shape Optimization Part I and II", Von Karman Institute, Brussels, Belgium, March 8, 2006.

25. K. Palaniappan, P. Beran and A. Jameson, "Optimal Control of LCOs in Aero-Structural Systems", 2nd AIAA Multidisciplinary Design Optimization Specialist Conference, Newport, RI, May 1-4, 2006.

26. A. Gopinath, P. Beran and A. Jameson, "Comparative Analysis of Computational Methods for Limit-Cycle Oscillations", 47th AIAA Structures, Structural Dynamics and Materials Conference, AIAA Paper 2006-2076, Newport, RI, May 1-4 2006.

27. S. Hazra and A. Jameson, "One-Shot Pseudo-Time Method for Aerodynamic Shape Optimization Using the Navier-Stokes Equations", 45th AIAA Aerospace Sciences Meeting & Exhibit, AIAA Paper 2007-1470, Reno, NV, January 8-11, 2007.

Unstructured Methods for Analysis and Design of Viscous Flows

In this section we report our progress towards a new platform for computational aerodynamics analysis and design on arbitrary meshes. The approach was designed for maximum flexibility to serve as the basis for a future industrial strength flow solver on general grids, and as a framework for advanced research in the area of CFD and aerodynamic design. Such a flexible platform is crucial for transfering new research to industrial applications. We briefly describe the capabilities and methods and show results from initial validation on inviscid and viscous test cases. The research addresses open issues in CFD on unstructured grids such as viscous discretization and multigrid methods in an unstructured context.

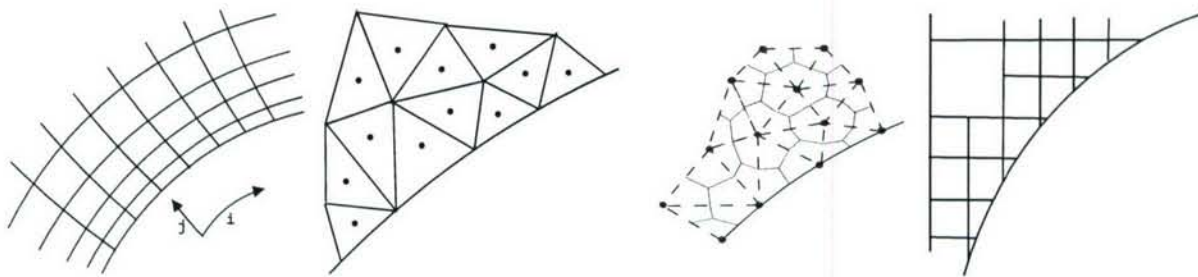## Support for Arbitrary Meshes and Different Discretization Techniques

Figure 1: Examples of different mesh types and discretization techniques. From left to right: Structured, unstructured in cell-centered discretization (variables are stored at the cell-centers), unstructured in cell-vertex discretization using the median dual (variables are stored at the nodes), Cartesian.

Different types of meshes (structured, unstructured, Cartesian) as well as conceptually different methods of discretization are used in computational fluid dynamics today. Examples of discretization techniques are cell-centered discretization or cell-vertex discretization with one of the possible ways to define dual meshes from a given primary mesh topology. Figure 1 illustrates different mesh types and different discretization techniques.
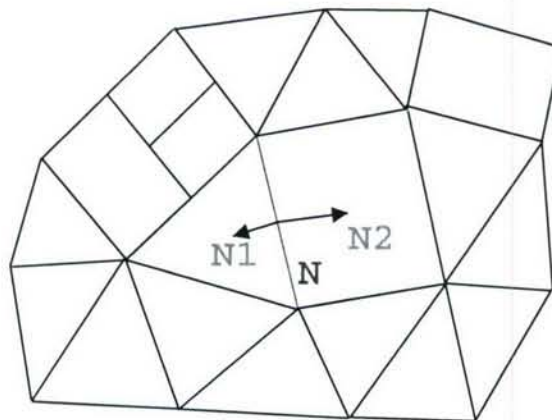

Figure 2: Two dimensional illustration of the face-based data structure.

```
do i=ncell1,ncell2
   set residual(i) to zero
end do

do n=nface1,nface2
   N1      = ncf(1,n)
   N2      = ncf(2,n)
   flux(N)      = f(solution(N1),solution(N2))
   residual(N2) = residual(N2)  +flux(N)
   residual(N1) = residual(N1)  -flux(N)
end do

do i=ncell1,ncell2
   solution(i)  = solution(i)  -residual(i)
end do
```
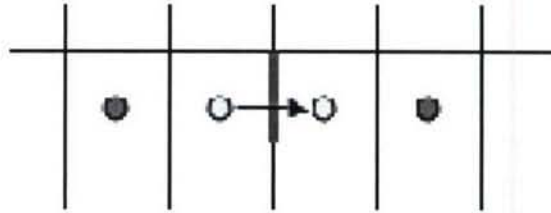
Figure 3: Basic solution algorithm in Flo3xx

Figure 4: Stencil for 2nd order flux computation on a structured mesh.

The newly developed method can operate on any of the above mesh types and discretization techniques. In fact, the flow solver module is at present completely indifferent to the underlying mesh topology so that it can run, in principle, on arbitrary meshes. A face-based data structure is used, which recognizes pointers from cell interfaces to adjacent nodes as the only connectivity information. This is illustrated in Figure 2. Regardless of the mesh topology, there will always be a finite number of interfaces separating exactly two control volumes, including halo cells at boundaries. By looping over these interfaces all necessary flux computations can be carried out. The pseudo-code in Figure illustrates the basic algorithm used in the flow solver module. While this algorithm is simple, the connectivity information used is not normally the one stored in primary meshes. Computational complexity is shifted to the preprocessing stage, where the necessary data structure is generated along with metric data. Currently, preprocessing is implemented to provide metrics for the median dual mesh and the primary mesh for the four most common element types tetrahedra, prisms, pyramids, and hexahedra.

Preprocessing for hexahedra allows the treatment of structured meshes in an unstructured context. For structured meshes the data structure can also be augmented to recover the treatment that is normally used for this type of mesh. Figure 4 illustrates the usual stencil used for a second order flux computation on a structured mesh. The blue cell centers in Figure 4 are pointees of the face between them in an unstructured context. By creating an additional level of pointers to the next-but-one neighbors (green cell centers), it is possible to reproduce the structured algorithms with the unstructured code. Note that there are thus two ways in which structured meshes can be treated. One way is to look at them as unstructured hexahedral meshes and use a general-mesh treatment, involving gradient reconstruction (to be described below). Another way is to use the described extra data structure to reproduce the exact structured algorithms, which is faster compared to first method. It also serves to asses the minimum overhead that is incurred compared to a structured code due to the indirect addressing. Numerical experiments have shown this overhead to be around 25%.

Cell-centered discretization using the primary mesh or cell-vertex discretization using the median dual mesh can be selected at run-time, the only difference being the preparation of the metric data. Usually, subtle differences between cell-centered and cell-vertex discretization exist even in a mesh transparent flow
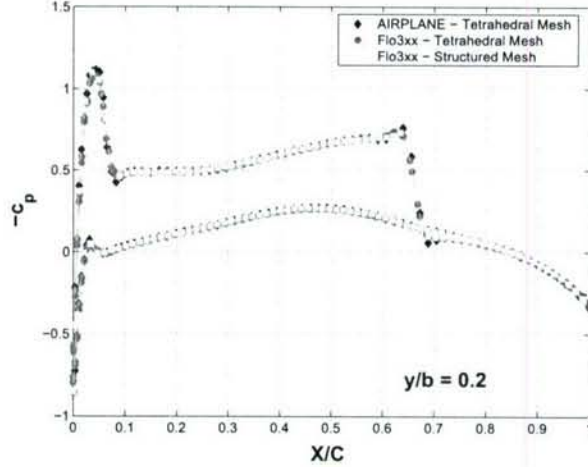
Figure 5: Pressure distribution in the wing section $y/b = 0.2$ for the Onera M6 wing at Mach number $M = 0.84$ and $\alpha = 3.06°$ angle of attack. Results are shown for a structured mesh with 1.1 million nodes and for a tetrahedral mesh with 316,000 nodes.

solver module, for example at the boundaries. In this implementation a unified treatment of the boundaries has been chosen, using halo-cells at boundaries for any kind of mesh, i.e. for cell-vertex schemes boundary conditions are not enforced at the nodes. During preprocessing boundary nodes become dual cell centers, which are no longer located on the boundary, but shifted to the dual cell centroids. The construction of halo cells proceeds in the same manner as for cell-centered discretization.

Inviscid Validation

Figure 5 provides initial validation of the unified-mesh algorithm. Both a structured mesh with approximately 1.1 million nodes and an unstructured tetrahedral mesh with 316,000 nodes have been used to calculate the flow for the Onera M6 test case at Mach number $M = 0.84$ and $\alpha = 3.06°$ angle of attack. The c_p distribution at the wing section $y/b = 0.2$ is compared to results obtained with the solver AIRPLANE on the same unstructured tetrahedral mesh. All computations have been carried out using cell-vertex discretization on a three-level multigrid sequence.

Viscous Discretization

Since gradients are needed for state reconstruction they are initially computed for the nodes of the primary mesh or the centroids of the primary elements, depending on the discretization type chosen. For viscous dicretization the gradients must be evaluated at the interfaces between adjacent cells. This can be done by a suitable average, which typically depends on the mesh structure and choice of control volume. Since the goal for the computational platform is complete mesh transparency, this dependence on the mesh topology is unsatisfactory.

In the current implementation gradients are constructed using either the unweighted least-squares method or a gauss-type reconstruction, i.e.

$$\nabla w_i = \frac{1}{V_i} \int_A \bar{\phi} \, dA \tag{1}$$

where V_i is the cell volume, and the overbar denotes a suitable face average.

6

For conventional viscous discretization an initial value for the gradient at the cell interface may be obtained by averaging the values of adjacent cells, ϕ_i and ϕ_j, to give

$$\overline{(\nabla\phi)_{ij}} = \frac{1}{2}\left[(\nabla\phi)_i + (\nabla\phi)_j\right]. \tag{2}$$

Subsequently a correction in the direction $\vec{s}_{ij}$ is applied to avoid odd-even decoupling, where

$$\vec{s}_{ij} = \frac{\vec{r}_j - \vec{r}_i}{|\vec{r}_j - \vec{r}_i|}.$$

This leads to the following gradient on the interface

$$(\nabla\phi)_{ij} = \overline{(\nabla\phi)_{ij}} - \left[\overline{(\nabla\phi)_{ij}}\cdot\vec{s}_{ij} - \frac{\phi_j - \phi_i}{|\vec{r}_j - \vec{r}_i|}\right]\cdot\vec{s}_{ij}. \tag{3}$$

This modification results in a stable discretization of the viscous terms and does not affect the accuracy as long as the interface integration point is located halfway between the two cell-centers. This, however, is only the case for the median dual control volume, rendering this type of viscous discretization highly mesh dependent.

Using concepts of kinetic gas theory, viscous discretization can be accomplished in a different fashion. Many researchers have used the Boltzmann equation or its BGK simplification, i.e. the BGK equation, as a basis for the construction of numerical fluxes. Firstly we note that the Navier-Stokes equations can be obtained by Chapman-Enskog expansion of both the full Boltzmann equation as well as the BGK equation, the difference being only in the values of the transport coefficients.

For more details of the actual discretization used, the reader is referred to the appropriate publication at the end of this report. The details have been omitted here for conciseness.

For initial validation we provide the solution of a resolved shock structure obtained with the new scheme, see Figure 6. It should be pointed out at this point that, since the Chapmann-Enskog expansion of the BGK
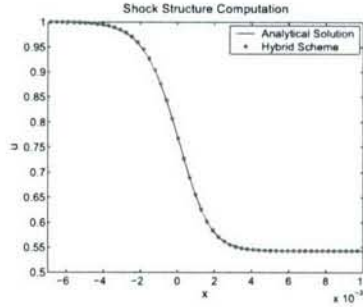
Velocity distribution across a normal shock.
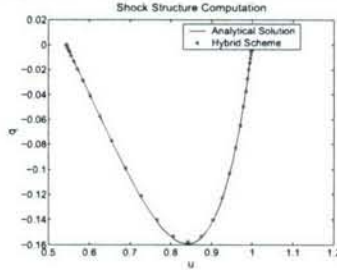
Heat flux across a normal shock.

Figure 6: Resolved shock structure for upstream Mach number $M = 1.6$ and a Prandtl number of $Pr = 0.72$

equation gives the transport coefficients as a sole function of the collision time τ, only one parameter can

7

be set automatically to the right value. This will usually be the dynamic viscosity. For accurate heat flux computations, the reconstruction involving the temperature gradient has to be scaled appropriately, so as to correspond to the correct Prandtl number.

For further validation consider a zero-pressure-gradient boundary layer. Figures 7 shows that the solution computed is in close agreement with the Blasius solution.

A detailed description of this research is given in the thesis of Georg May, entitled "A Kinetic Scheme for the Navier-Stokes Equations and High-Order Methods for Hyperbolic Conservation Laws". During the period of his thesis research Georg May received support from a Stanford Graduate Fellowship.
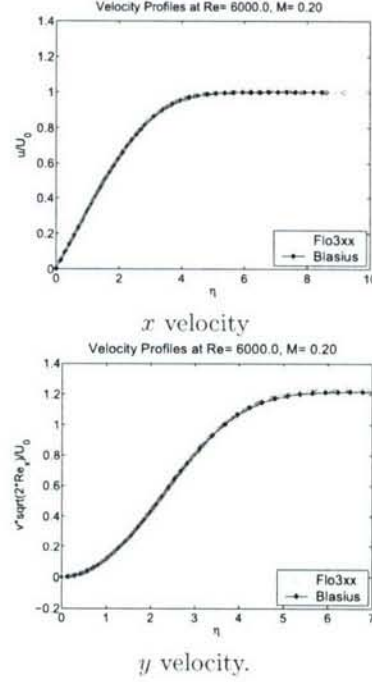

x velocity

y velocity.

Figure 7: Laminar Boundary Layer at $Re = 6000$ and $M = 0.2$ using the JST scheme and direction-corrected central discretization of the viscous terms.

Planform Optimization Studies Using Viscous Flows and a Weight Estimation Method

In this section we focus on our work on aero-structural optimization of wings for long range transport aircraft, using adjoint-based optimization techniques. We are interested in exploring and comparing the attainable trade-offs such as L/D vs. Mach number, which may be appreciable higher than the historical trends typically used in conceptual design. We also seeks to identify a discernable trend in the variation of planform variables such as sweep, thickness-to-chord ratio, aspect ratio, and chords for optimum wings. Results form wing-fuselage and complete-aircraft-configuration optimizations indicate that stretching the span together with decreasing the sweep and thickening the wing sections, the lift-to-drag ratio can be increased without any penalty on the structure weight.

The methodology used for this weight-estimate-based optimization studies has been presented earlier and will not be repeated here. The reader is referred to the publications by Leoviriyakit and Jameson listed at the end of this report.

Redesign of the Boeing 747 wing

We present a result to show that the optimization approach we are pursuing can successfully trade planform parameters and wing weight. We also demonstrate how to apply strategy game theory to gradient based optimization.

Here, the case chosen is the Boeing 747 wing fuselage combination at Mach 0.87 and a lift coefficient $C_L = 0.42$. The computational mesh is shown in Figure 8.

In this test case, the Mach number is the current normal cruising Mach number of 0.85. We allowed section changes together with variations of sweep angle, span length, chords, and section thickness. Figure 9(a) shows the baseline wing. Figure 9(b) shows the redesigned wing. The parameter $\frac{\alpha_2}{\alpha_1}$ was chosen such that the cost function corresponds to maximizing the range of the aircraft. Here in 30 design iterations the drag was reduced from 137 counts to 117 counts and the structural weight was reduced from 498 counts (80,480 lbs) to 464 counts (75,000 lbs). The large reduction in drag is the result of the increase in span from 212.4 ft to 231.7 ft, which reduces the induced drag. The redesigned geometry also has a lower sweep angle and a thicker wing section in the inboard part of the wing, which both reduce the structural weight. Moreover the section modification prevents the formation of shock. The baseline and optimized planforms are shown in Figure 9(c). Overall, the re-design with variation planform gives improvements in both aerodynamic performance and structural weight, compared to the previous optimization with a fixed planform.

Redesign of the BAe MDO DATUM wing

To further validate this planform-and-section trend, we selected the BAe MDO DATUM wing, a wing that has been designed with relatively modern tools. At its cruising Mach .85, this wing has low sweep angle and high thickness-to-chord ratio sections.

This test case presents a technical challenge to the optimization because the BAe and B747 are designed to operate at the same flight condition and their planforms are sized in the same range. However the original sweep of BAe is already smaller than the optimum sweep of B747 and its wing span is already longer than the optimum span of B747.

Figures 10(a), 10(b), and 10(c) show the original wing, optimized wing, and their planforms respectively. Despite of low-sweep, long-span, and thick-wing-sections of the original wing, the optimal wing has less sweep,
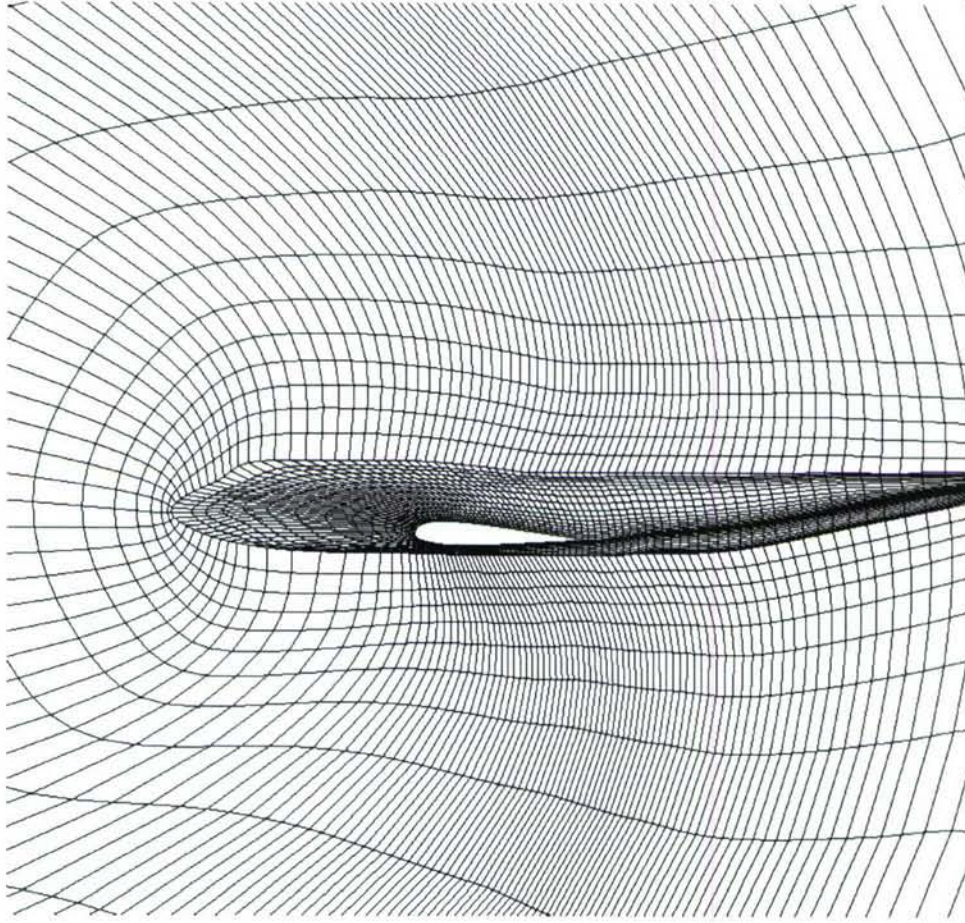
9

Figure 8: Computational grid of the B747 wing fuselage

longer span, and thicker wing sections. But the changes in the planform are not large. With these changes, the optimum wing shows improvement in both drag and weight. The drag is reduced from 164 counts to 145 counts, and the weight is reduced from 480 counts (87,560 lbs) to 476 counts (86,980 lbs). This optimized BAe wing strongly agrees with the trend suggested from the B747 and MD11 cases.

This research is documented in the thesis of Kasidit Leoviriyakit, entitled "Wing Planform Optimization via an Adjoint Method".

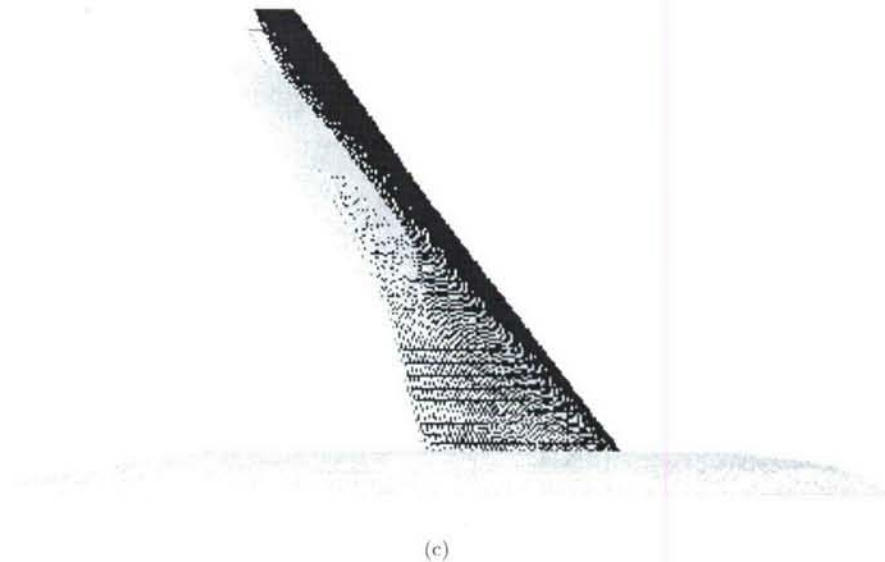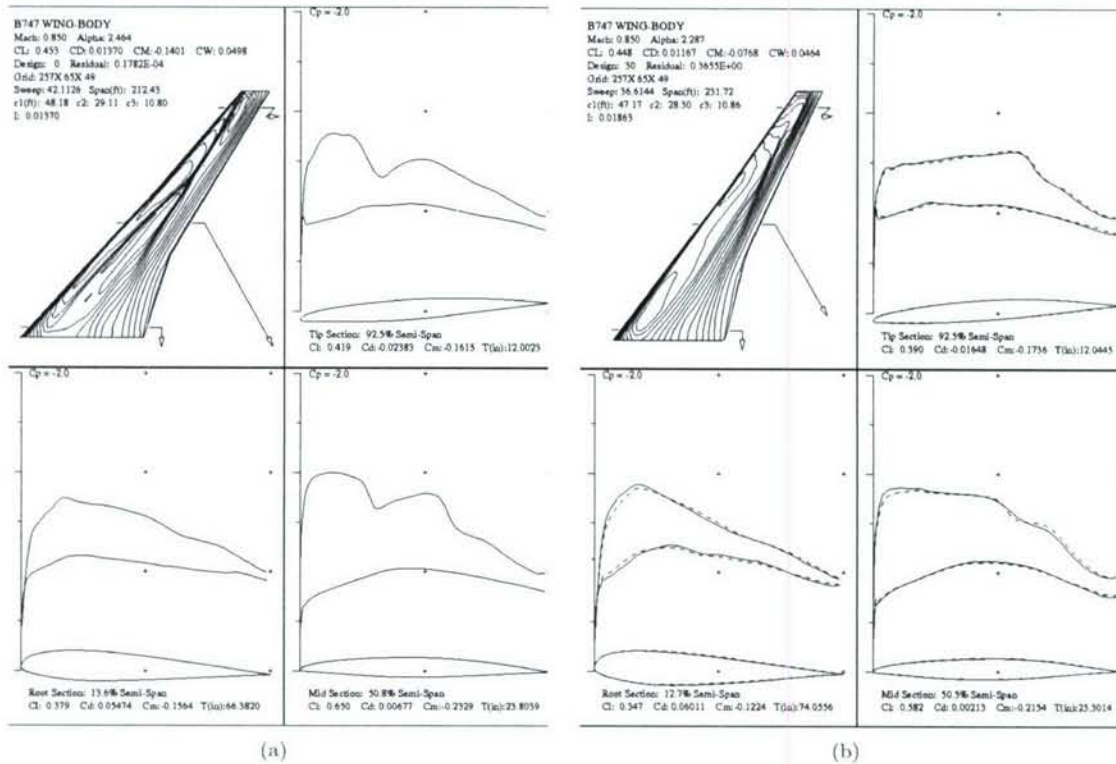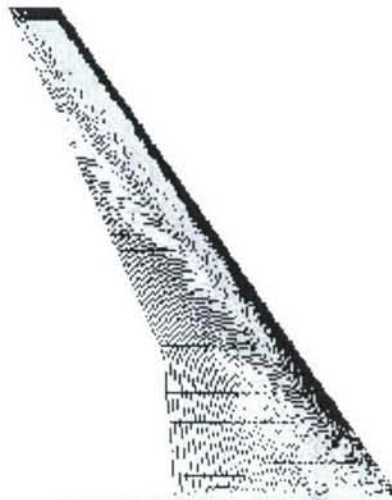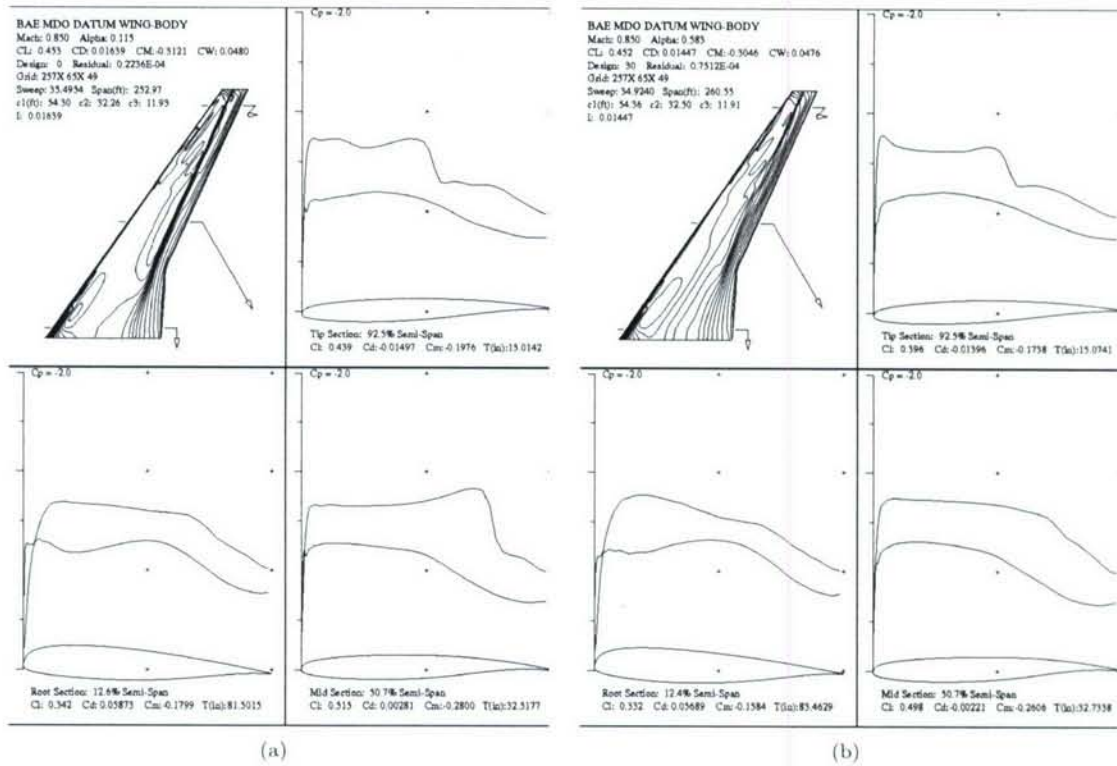(a)   (b)

(c)

Figure 9: Redesign of Boeing 747 wing, using section and planform modifications. The optimum wing has longer span, less sweep, and thicker wing sections. We also over-plot the optimum planform form our inviscid calculation to indicate good agreements between the inviscid and viscous optimizations. Top left: baseline. Top right: Optimized. Planform (Baseline : Green, Optimum : Blue).

(a)

(b)

(c)

Figure 10: Redesign of BAe MDO DATUM wing, using section and planform modifications. The optimum wing has longer span, less sweep, and thicker wing sections.

12

Two-Level, Multi-Fidelity Approach to Multi-Disciplinary Design of Supersonic Aircraft

The *conceptual/preliminary* design of supersonic aircraft configurations requires a multi-disciplinary approach that provides the designer with information regarding the key trade-offs between the disciplines participating in the design. At the same time, at these stages of the design, the available tools must provide a level of flexibility that permits the exploration of large areas of the design space with significant changes to a baseline configuration. In order to achieve credible results one would like to use high-fidelity modeling tools for all of the components (and interactions) of the design. This can, however, be prohibitively expensive and in addition, it may significantly decrease the ability to make drastic modifications to the aircraft configuration in question. As our work has progressed in this area, we have come to realize that a truly hybrid, multi-fidelity approach that is properly managed is one of the answers to the supersonic design problem. We are currently pursuing a two-level approach to the design of a supersonic business jet configuration where we combine a conceptual, SIMPLEX-based, low-fidelity optimization tool with a hierarchy of flow solvers of increasing fidelity (including simplified aerodynamic models, a linearized panel method and both structured and unstructured Euler solvers) and advanced adjoint-based Sequential Quadratic Programming (SQP) optimization approaches. Although this kind of aircraft has been studied in the past within the context of low supersonic boom, in this work we focus on the aerodynamic performance aspects alone: no attempt is made to reduce the acoustic signature since this has not been a driver in military applications of this technology. The results show that this particular combination of modeling and design techniques is quite effective to produce designs with optimum performance that meet or exceed all of the design constraints of the problem. In addition, we show that high-fidelity aerodynamic shape optimization techniques for complex configurations (such as the adjoint method) can be effectively used within the context of a truly multi-disciplinary design environment.

In this work, we combine ideas of multi-fidelity analysis and design and a two-level optimization procedure into a hybrid concept that includes:

1. The Program for Aircraft Synthesis Studies (PASS): a multi-disciplinary design tool that incorporates carefully tuned fast models for the various disciplines in the design and is able to deal with all the major objective functions and constraints in typical aircraft synthesis problems.

2. A hierarchical, multi-fidelity response surface generation technique that uses results from classical supersonic aerodynamics, a linearized supersonic panel code (A502/Panair), and unstructured adaptive Euler solver (AirplanePlus) to create models of the aerodynamic performance.

3. Automated tools based on a common geometry database to drive the analysis tools that are used in the generation of the response surfaces in this problem (BOOM-UA). This CAD-to-solution procedure is based on the CAPRI CAD-interface of Haimes, the A502/Panair and AirplanePlus flow solvers, and the Centaur mesh generation system.

4. Adjoint aerodynamic shape optimization tools for both single-block wing-body configurations (SYN87-SB) and multiblock complete configurations (SYN107-MB) that use inexpensive gradient calculations with larger numbers of design variables to modify the twist and camber distributions of the wing (without changes to the wing planform) and to achieve the highest aerodynamic performance.

More details of each of the components of this work can be found in the appropriate publications listed at the end of this report.

A typical unstructured surface mesh for the types of aircraft configurations in question can be seen in Figure 11 below. The resulting flow solution is shown in Figure 12.
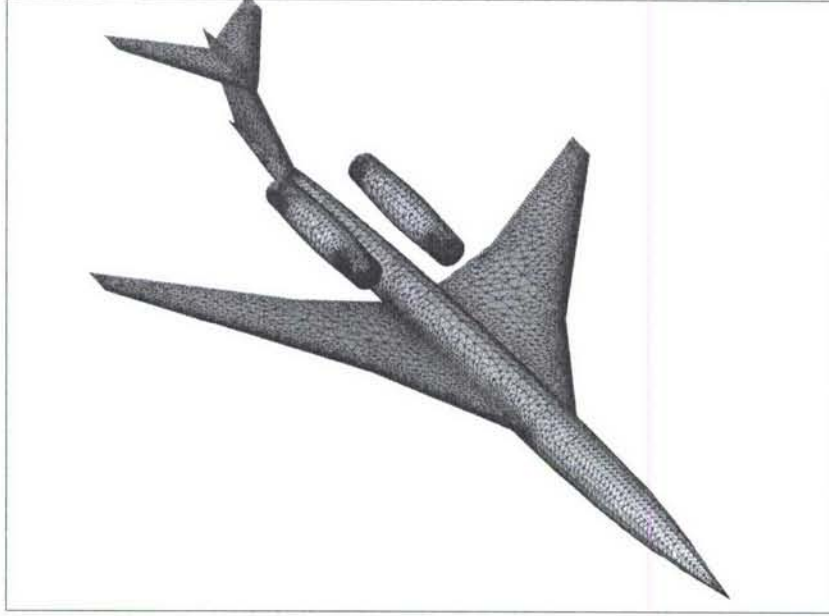
Figure 11: Unstructured tetrahedral surface mesh around full baseline configuration

Multi-fidelity, Multi-Discipline Design Approach

This section explains the procedure we have used to integrate the tools described above into a single analysis and optimization capability. The concept is straightforward: if the multi-fidelity analysis capability can be used to create response surfaces for the drag coefficient, C_D, the corresponding low-fidelity modules in PASS can be replaced by these response surface fits. This makes for a remarkably simple integration problem and also provides us with the ability to predict the changes in aerodynamic performance resulting from wing section changes. The baseline version of PASS is unaware of the actual wing sections used and assumes that, whatever the sections are, they have been adjusted in such a way that the camber and twist distributions are optimal (in the sense that they get close to elliptic load distributions in both the spanwise and streamwise directions). PASS can then be used to generate optimized results and the outcome of the optimization can be analyzed using the high-fidelity tools to ensure that the response surface fits provide accurate representations of the true high-fidelity responses. The level of accuracy in the response surface representation depends greatly on the number of high-fidelity calculations that are used. Since we are trying to minimize this number, we will undoubtedly incur some errors in the fits. The validity of these fits is typically assessed by direct analysis of the resulting optimized designs using two different Euler solvers.

Our multi-fidelity approach to the construction of the response surface fits relies on a hierarchy of three different aerodynamic analysis modules

1. PASS internal analysis based on classical aerodynamics.

2. A502/Panair supersonic linearized panel code.

3. Euler solutions of the highest fidelity using unstructured mesh (with a total of around 1-2 million nodes for the complete configuration) - we refer to these computations by the label "Fine Euler (FE)."

In order to obtain response surface fits of the highest fidelity one could carry out a large number of FE solutions and fit the resulting data. Unfortunately, for large dimensional design spaces (we will be using a total of 23 design variables later on), accurate fits require a large number of function evaluations. This is particularly true in our case since the ranges of variation of each of the design variables will be rather large.
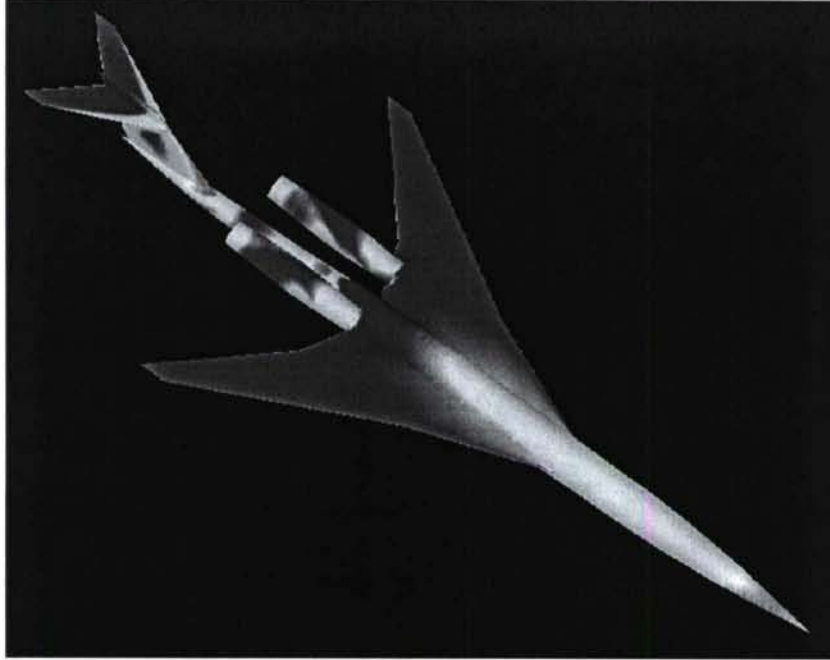
14

Figure 12: Upper surface pressure distribution for full baseline configuration using AirplanePlus Euler calculation.

The main objective in this section is to generate response surface fits of the same quality/accuracy that would be obtained by evaluating the FE solutions only, but at a much reduced cost. We accomplish this by relying on a fundamental hypothesis that will be tested later on: *the higher fidelity tools are only needed in small regions of the design space where the lower fidelity models have exhausted their range of applicability.* This is bound to be true as it is the premise upon which aerodynamic design has been predicated for the last 50 years: aerodynamicists and engineers use the fastest tools for a specific purpose (when they are known to work well) and switch to more time-consuming, expensive tools only when they are needed. For example, in supersonic design, classical equivalent area concepts and linearized panel codes can provide very accurate results as long as non-linear effects (such as transonic flows in the direction normal to the leading edge of the wing) are not present and viscosity does not play a dominant role in the solution of the flow.

With this in mind, we have used the following five-step procedure to create the response surfaces used in this work. All databases of candidate designs are obtained by populating the design space using a Latin Hypercube Sampling (LHS) technique.

1. Run a large database of candidate designs ($> 8,000$) using the aerodynamics module in PASS. Each evaluation takes roughly 1 second to compute on a modern workstation (Pentium 4, 3.2 GHz). This evaluation also flies each aircraft through the mission and returns a measure of the infeasibility of the design (an L-2 norm of the constraint violations.) Those designs that are found to significantly violate the requirements/constraints of the mission are removed from the database and are no longer considered in the response surface creation.

2. Run the remaining database of candidate designs ($\approx 2,500$) using the A502/Panair solver. Each evaluation requires about 10 seconds of CPU time on the same modern workstation.

3. Select the design points whose relative error for C_D (based on the baseline design) is larger than a specified threshold, $\epsilon_{PASS-A502}$, and analyze only those designs using the Fine Euler (FE) approach. In our work, we have set this threshold to about 45 % resulting in a number of high-fidelity function evaluations in the neighborhood of 200. Each FE evaluation, from beginning to end, including geometry and mesh generation(the bottlenecks in the process, since they are run serially) requires about 40

15

minutes of wall clock time. The flow solution portions (using AirplanePlus) are run in parallel using 16 Athlon AMD2100+ processors of a Linux Beowulf cluster.

4. A baseline quadratic response surface fit (using least squares regression) is created for the C_D obtained with A502/Panair. The error between the values of the FE evaluations and the predictions of these quadratic fits is approximated with a Kriging method, and the resulting approximation is added to the baseline quadratic fits.

In sum, the response surfaces provided to PASS are the addition of the quadratic fits based on the A502/Panair results and the Kriging fits of the error between the FE solutions and those quadratic fits.

Figure 13 shows the result of the over 2,500 candidate designs (green dots) evaluated using A502/Panair that are retained after the initial filtering of over 8,000 PASS results. The red dots in the Figure indicate those candidate designs for which the predicted values of C_D are off by more than $\epsilon_{PASS-A502} > 45\%$ between PASS and A502. Note that a number of these red dots have unreasonably large values of C_D since the geometries and design conditions are such that the limits of applicability of A502 are exceeded. These points for which the disagreement between PASS and A502 is large are taken for further evaluation using FE. Figure 14 shows in blue the results of the FE analyses for a subset of about 200 of the red A502 results. The final result is a set of FE evaluations that are meant to be clustered around the areas where the lower fidelity models cannot accurately predict the flow physics.
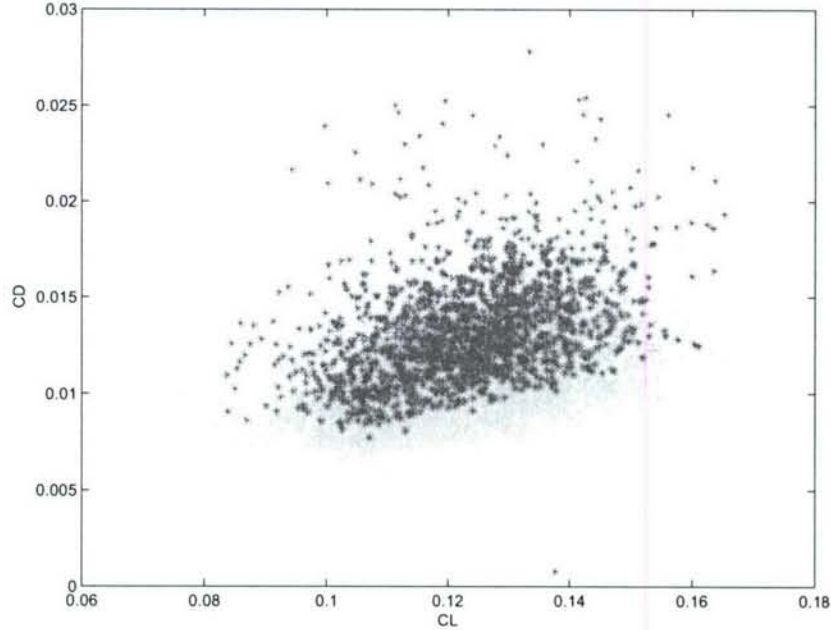

Figure 13: Database of PASS (green) and A502/Panair (red) results.

This multi-fidelity procedure has, to some extent, the flavor of Richardson's extrapolation in that it recursively uses results from different fidelities to arrive at a final answer/fit. It also has an adaptive nature to it, as results from the higher fidelity models are only evaluated in areas of the design space where the lower fidelity models are found to be insufficiently accurate. If the hierarchy of models is chosen in such a way that the areas where the lower fidelity models fail are small compared with the size of the design space, then the procedure described above should be quite effective in producing results that are of nearly high-fidelity over the *entire* design space. Our experience shows that this is the case for aerodynamic performance: the PASS aerodynamic module is quite good at predicting the absolutely best wing (lower bound estimate on the C_D) that could be produced if considerable design work were done on the configuration (potentially using adjoint methods and a high-dimensional shape parameterization). However, it is unable to predict
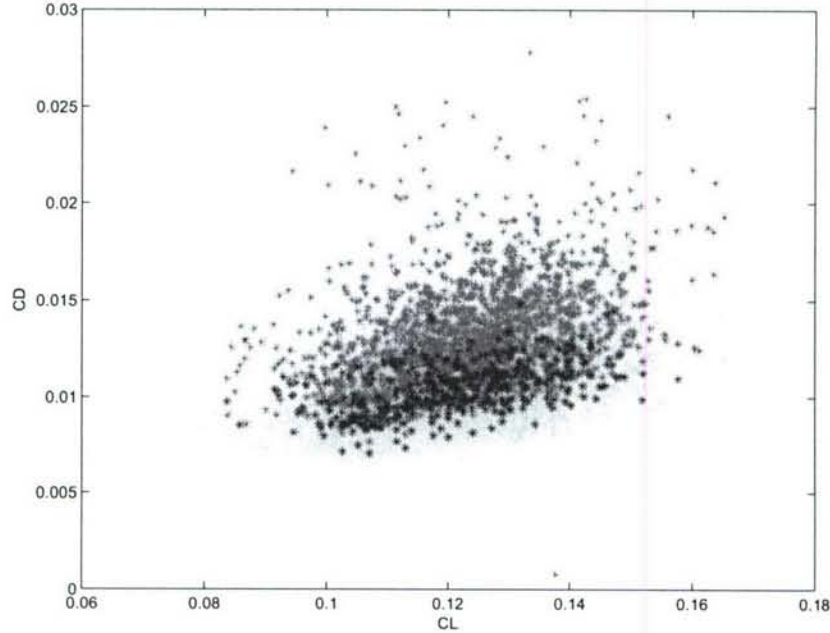
16

Figure 14: Database of PASS (green), A502/Panair (red) and FE (blue) results.

some of the finer details of aerodynamic performance and certainly fails when transonic effects are present. A502/Panair is also unable to deal with transonic flow effects but produces more realistic results than the PASS analysis as the actual geometry of the configuration is truly accounted for. Finally, the Euler models are quite good predictors of the aerodynamic performance of the complete aircraft as long as viscous effects are not dominant. It must be mentioned that, since sonic boom has not been considered in these designs, the Coarse Euler (CE) evaluations which we have used in previous work would be sufficient as the differences in C_D between CE and FE calculations were found to be small (less than 5 counts) over the large range of variations pursued in this work.

Second Level Optimization: Complex Configuration Adjoint Method

Non-gradient based methods (direct searches, simplex method, genetic algorithms) have been shown to work with a wide range of problem types, and the additional complexity required to compute gradients, approximate Hessians, perform line searches and determine the optimal steps, is not needed. These properties have a tendency to make this search procedures simple and robust.

In addition, these search procedures are able to handle rather noisy and large design spaces, making them a reasonably good match for conceptual design procedures, as was mentioned in the Introduction. However all of these algorithms tend to require a very large number of function evaluations for convergence and therefore their computational cost can be very high.

On the other hand, if a design problem shows a smooth response to the variation in the design variables and gradient information is readily available and can be obtained inexpensively (as is the case with the adjoint method) gradient-based optimization techniques can be shown to have significant advantages over non-gradient search procedures.

In our approach we are seeking to combine the advantages of both gradient- and non-gradient-based optimization procedures. As mentioned earlier, PASS uses a simplex method and is able to produce reasonable designs (using a maximum of around 20-25 design variables) even with very large variations of the design variables. Once the simplex method has converged to an optimum (local or global) we may limit ourselves to

Cruise Mach	1.6
Range	4,000 nmi
BFL	6,500 ft
Minimum static margin	0.0
Alpha limit	15°
MTOW	96,876 lbs

Table 1: Performance requirements for optimized baseline configuration.

smaller changes in the configuration. These changes are more likely to result on well-behaved design spaces that can be tackled with an adjoint procedure and a gradient-based optimization algorithm.

In this second level of our optimizations we limit ourselves to modifications in the twist and camber of the wing, while maintaining the same wing planform, fuselage and relative positioning of the nacelles and empennage.

Two different tools are available for this portion of the overall optimization:

1. *SYN87-SB*. A single-block, wing-body Euler adjoint optimization code that uses the NPSOL SQP algorithm for the optimization with or without constraints. SYN87-SB allows for arbitrary changes to the shape of the fuselage and wing and is able to enforce thickness, curvature, and fuel volume constraints.

2. *SYN107-MB*. A multi-block, complete configuration, RANS adjoint optimization code that also uses the NPSOL SQP algorithm for optimization and that allows similar geometry controls, cost functions, and constraints as SYN87-SB, but that can be made to treat arbitrarily complex geometries such as the complete aircraft configurations that are the subject of this work.

Optimization Results

For subsequent design work, an optimized baseline geometry was generated by running the standard version of PASS for a mission with the performance objectives summarized in Table 1. Mission requirements and geometric constraints for the baseline configuration were based on numbers that were felt to be representative of current industry interest. The value of the MTOW is the result of the optimization as this was the objective function of the design. As mentioned before, in an effort to generate an aircraft achievable using current levels of technology, advanced technology assumptions were kept to a minimum.

The values of the design variables for the resulting baseline configuration (which are also used as starting points for subsequent designs) are provided in Table 2. Note that the values highlighted in red were not allowed to vary during this initial optimization. In addition to these variables, 6 variables representing the radii of fuselage stations located at 5%, 10%, 15%, 62.5%, 75%, and 87.5% of the fuselage length were added to allow for performance improvements and to maintain cabin and cockpit compartment constraints. Finally wing section changes were allowed at three defining stations. The twist at the root/symmetry plane section, the leading edge crank section and the tip section were allowed to vary. Furthermore, the value of the maximum camber and the location of maximum camber were also allowed to change at the first two wing defining stations. This makes up for an addition 7 design variables for the wing.

High-Fidelity Validation of Optimization Results

The aerodynamic performance of the configurations predicted by PASS combined with the response surface fits should be validated with our high-fidelity tool, AirplanePlus. As mentioned above, although the results of the Euler validation are slightly different from what the fit predicted, the optimized configuration shows a good improvement in aerodynamic performance while satisfying all the mission requirements. A comparison of surface pressure distributions (for both the lower and upper surfaces and in side view) is shown below in
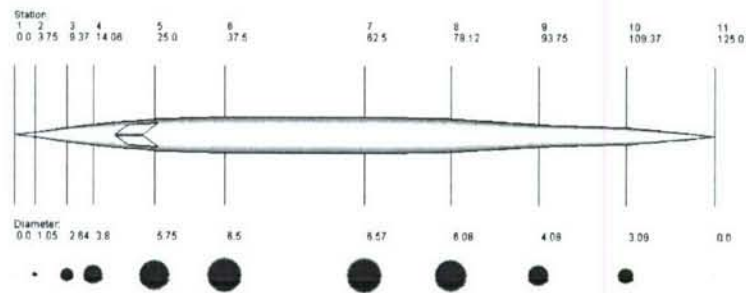
18

Wing and Tail Geometry

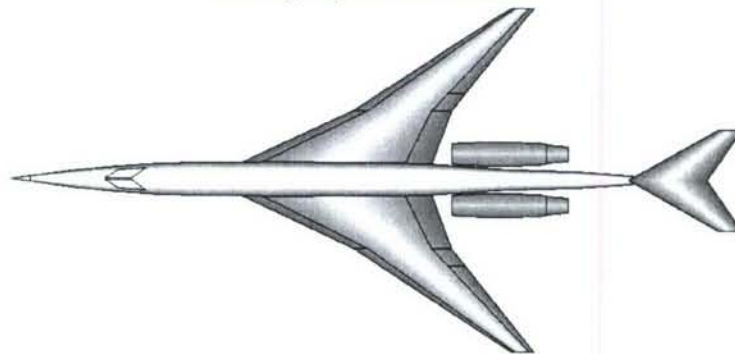|	
Wing reference area (S_{ref})	1,078 ft^2
Wing aspect ratio (AR)	4.0
Wing quarter-chord sweep (Λ)	53.35°
Wing taper	0.15
Wing dihedral	3°
Leading edge extension	0.278
Trailing edge extension	0.197
Break location	0.4
Location of wing root LE	0.294
Root section t/c	2.5%
Break section t/c	3.0%
Tip section t/c	2.5%
Vertical tail area (% S_{ref})	0.125
Vertical tail AR	0.65
Vertical tail Λ	56°
Vertical tail λ	0.6
Horizontal tail area (% S_{ref})	0.6
Horizontal tail AR	2.0
Horizontal tail Λ	56°
Horizontal tail λ	0.3

Fuselage Geometry

Maximum fuselage length	125 ft
Minimum cockpit diameter	60 inches
Minimum cabin diameter	78 inches
Cabin length	25 ft

Table 2: Geometric design variables for design optimization and values for baseline design.

Diameter:
0.0 1.05 2.64 3.8   5.75   6.5   6.57   6.08   4.08   3.09   0.0

Fuselage layout and stations

Top view of configuration

Final Cruise
t = 4.52 hrs
x = 4018 nmi
W = 49066 lbs
Mach = 1.6
alt = 54200 ft
L/D = 6.08
CL = 0.12
D/T = 1.09

Initial Cruise
t = 0.4 hrs
x = 246 nmi
W = 90824 lbs
Mach = 1.6
alt = 42002 ft
L/D = 6.49
CL = 0.13
D/T = 1.08

Acceleration
t = 0.11 hrs
x = 25 nmi
W = 94594 lbs
Mach = 0.77
alt = 35000 ft
CL = 0.42
D/T = 0.67

Climb
t = 0.13 hrs
x = 36 nmi
W = 94386 lbs
Mach = 1.12
alt = 35000 ft
CL = 0.2
D/T = 0.73

Take-off
T.O. Field Length: 5954
T.O. Weight: 96875

Landing
t = 4.52 hrs
x = 4018 nmi
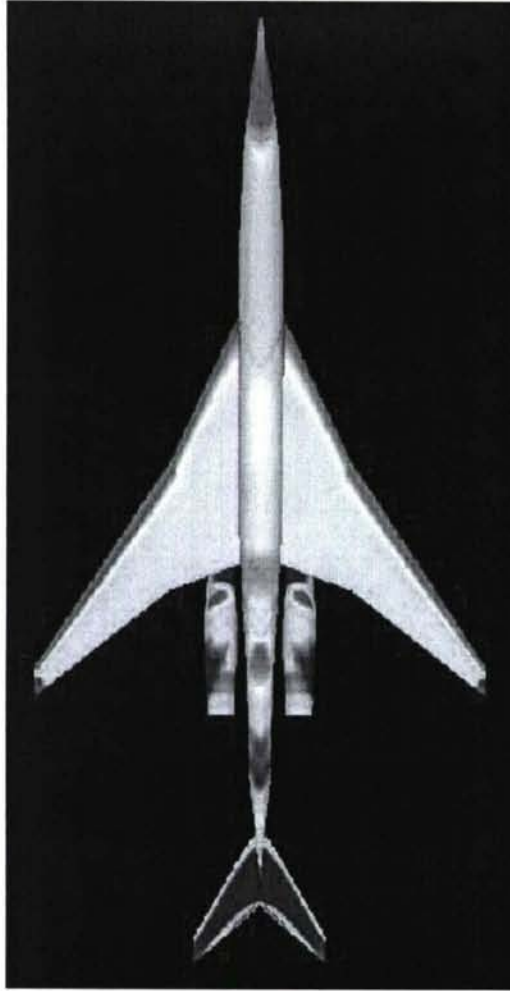W = 49066 lbs
Land Field Length = 4333 ft
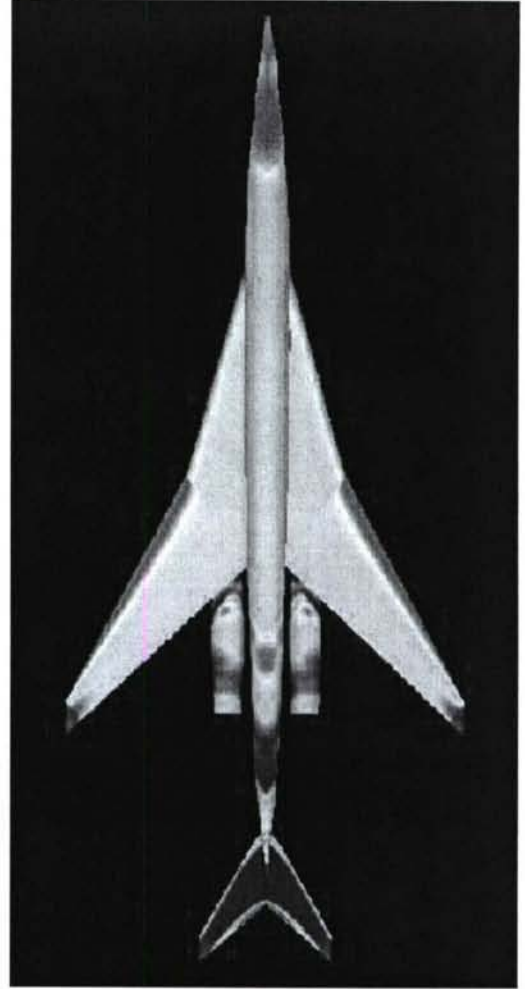
Mission profile

Figure 15: Summary of baseline configuration.

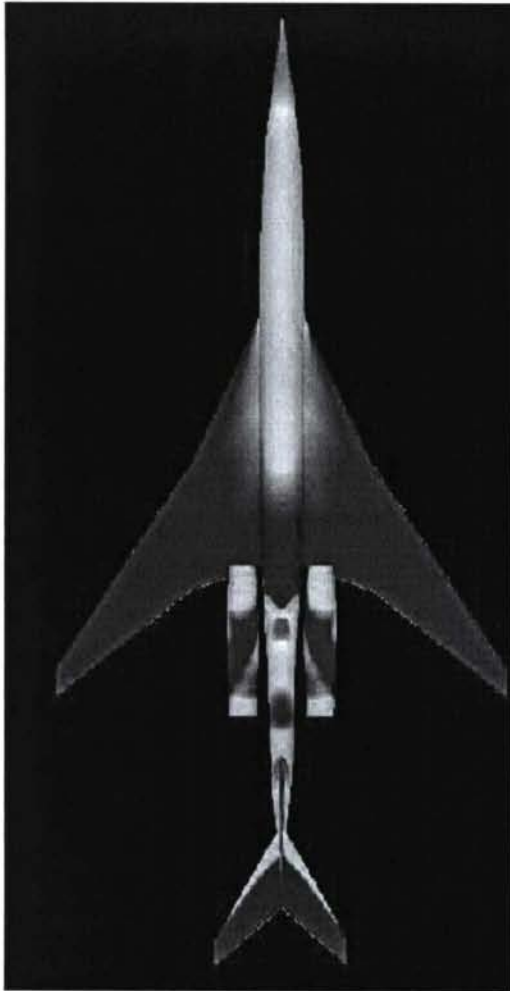Baseline configuration   Optimized configuration
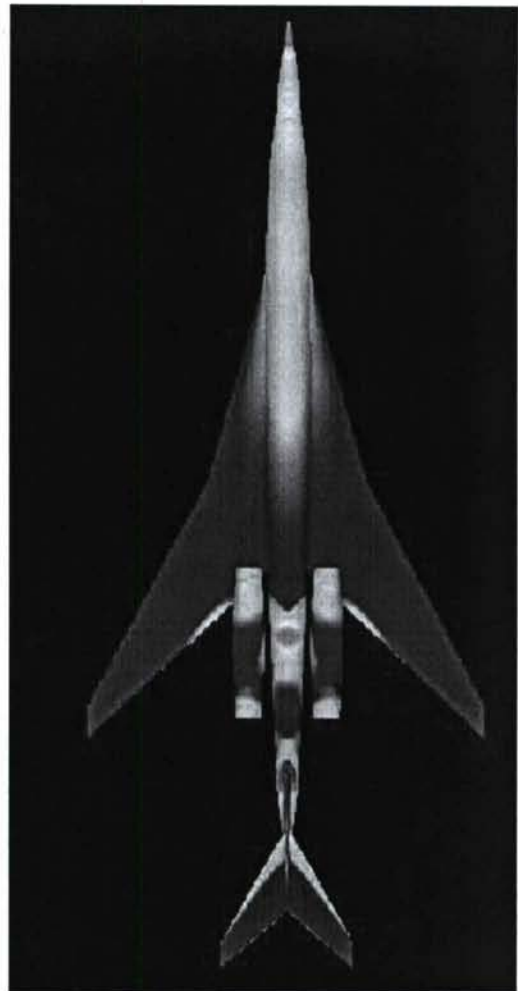
Figure 16: Pressure distribution plots - lower surface.

Figures 16, 17, and 18 The reader should notice a lightly larger fuselage radius around the nose area and increased wing inboard sweep which has reduced the shock strength significantly. We have also created a multiblock mesh with nearly 6 million nodes for the optimized configuration that we intend to use in future work for complete configuration adjoint designs. Given that this mesh was at hand, it provided us with a unique opportunity to cross-validate all of the Euler results that had been, up to then, produced with our unstructured flow solver, AirplanePlus. The results cannot be more satisfying since they provide nearly identical solutions throughout the range of C_Ls. This is important because the airfoils across the span of the configuration have rounded leading edges, but, because of the low thickness-to-chord ratios, it is quite hard to put enough grid resolution around the leading edge using nearly isotropic unstructured meshes. With the multiblock approach, anisotropic cells are easily created around the leading edge and can resolve the effects of leading edge curvature rather nicely. This means that the unstructured Euler solutions are just as capable of doing so. As an aside, we had thought earlier on that some of the discrepancies between the Euler solvers and A502 were due to the inability of the Euler solver to capture (with a coarse leading edge mesh) the leading edge suction. This drag polar comparison seems to indicate that this is not the case.

A detailed description of this research is given in the thesis of Seongim Choi, entitled "Multi-Fidelity Multi-Disciplinary Design Optimization of Supersonic Business Jets".
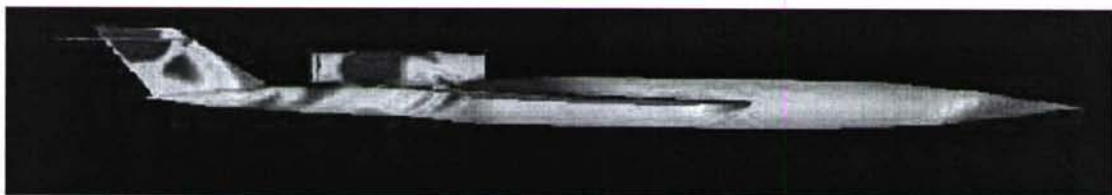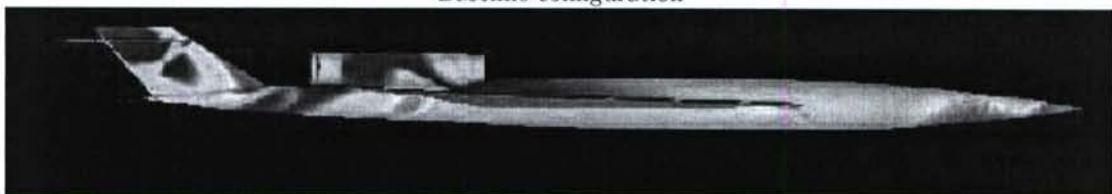
21

Baseline configuration

Optimized configuration

Figure 17: Pressure distribution plots - upper surface.

Baseline configuration

Optimized configuration

Figure 18: Pressure distribution plots - side view.

Algorithms for Automatic Feedback Control of Aerodynamic Flows

An airplane, by its very nature of design, is meant to be a flow control device. This becomes clear when one considers a steady air flow with and without the airplane. The very presence of the airplane alters the flow pattern, significantly so. Through the ages, the primary goal of the aerodynamicist has been to design airplanes such that they meet certain performance criteria. This could be, for example, the maximum range of the airplane or the drag at cruise conditions. Lower drag immediately translates to lower fuel consumption and hence lower operating costs.

The aerodynamic performance of an airplane is determined by the nature of the surrounding flow field under given flight conditions. The most important motivation for flow control arises thus:

If it becomes possible to control the nature of the surrounding fluid flow, then it is conceivable that both the operating envelope and the aerodynamic performance of an airplane within that envelope can be significantly enhanced.

Exploring techniques for active flow control has been the central theme of this research. All previous attempts at flow control have either involved designing simplistic controls for complex problems or complex *feedback* based controls for simple problems. Problems like separation control, drag reduction and control of the vortex shedding frequency in the flow past a cylinder have all been controlled using open loop controllers.

Closed loop control has been demonstrated only on simplistic models derived from simulation or experiment.

An *Ideal Flow Control Law* should have the following properties:

1. Broadly applicable: we are looking for an algorithmic framework for generating flow control laws for a variety of problems. The development of such a framework would enable easy analysis and design of control laws for a variety of flow control problems.

2. Scientific: the control laws should be based on a realistic model of the fluid system.

3. Robust:should account for variability in measurement, actuation, etc. This would mean that the control u should be *feedback* based

$$u = F(x), \tag{4}$$

where x is the current system state.

Our goal, therefore, is to develop *feedback* based control laws that are derived from a realistic representation of the flow. We try to make sure that the framework is as generic as possible, lending easy extension to a variety of situations. We then discuss specific applications of the control law thus derived, including control of Flutter.

Flow Control using Adjoint Sensitivities

Following along the lines of the argument made in the previous section, the Flow Control problem can be posed as the following optimization problem:

$$\text{Minimize: } I(\mathbf{w}, \mathbf{u}), \tag{5}$$

where $\mathbf{w}$ is the vector of state variables and $\mathbf{u}$ is the vector of control variables. I represents the quantity being controlled. It could be a measure of the drag, expressed as a difference between the current surface

pressure distribution and an *ideal* surface pressure distribution that has minimum drag. I could also be a measure of the deviation from an equilibrium condition. For example, in the case of flutter control, I is chosen to be a measure of the plunge and pitch of the wing. Minimizing I in this context is equivalent to bringing the system back to equilibrium.

The state vector $\mathbf{w}$ consists of the *Euler* state variables at each Finite Volume in the domain. Thus, if there are a million cells in the domain, the dimension of $\mathbf{w}$ is five million for a 3-D flow. The control vector $\mathbf{u}$ in our case, consists of the surface normal mass fluxes at every cell along the surface of the wing. The dimensionality of the control vector $\mathbf{u}$ is much smaller than that of the state vector $\mathbf{w}$.

The optimal control $\mathbf{u}$ is one that minimizes the cost function (5). The first derivative of the cost function with respect to the control variables $\mathbf{u}$ is

$$\frac{dI}{d\mathbf{u}} = \frac{\partial I}{\partial \mathbf{w}}^T \frac{\partial \mathbf{w}}{\partial \mathbf{u}} + \frac{\partial I}{\partial \mathbf{u}}. \tag{6}$$

While the second term is fairly straightforward to evaluate, the first is not. This is because the state $\mathbf{w}$ and the control $\mathbf{u}$ are related by the *Euler* equations which are of the form

$$R(\mathbf{w}, \mathbf{u}) = 0. \tag{7}$$

In the *Adjoint* framework, we do not evaluate the partial derivative $\frac{\partial \mathbf{w}}{\partial \mathbf{u}}$ explicitly. We first note that Equation (6) is identically zero. Therefore, it is permissible to multiply it by a Lagrange multiplier Ψ and add it to Equation (6). This gives

$$\frac{dI}{d\mathbf{u}} = \frac{\partial I}{\partial \mathbf{w}}^T \frac{\partial \mathbf{w}}{\partial \mathbf{u}} + \frac{\partial I}{\partial \mathbf{u}} + \Psi^T \left[\frac{\partial R}{\partial \mathbf{w}}^T \frac{\partial \mathbf{w}}{\partial \mathbf{u}} + \frac{\partial R}{\partial \mathbf{u}} \right]. \tag{8}$$

Rearranging the terms in Equation (8) we get

$$\frac{dI}{d\mathbf{u}} = \left[\frac{\partial I}{\partial \mathbf{w}}^T + \Psi^T \frac{\partial R}{\partial \mathbf{w}}^T \right] \frac{\partial \mathbf{w}}{\partial \mathbf{u}} + \left[\frac{\partial I}{\partial \mathbf{u}} + \Psi^T \frac{\partial R}{\partial \mathbf{u}} \right]. \tag{9}$$

Now Ψ is an arbitrary multiplier. We can choose it to make the coefficient of $\frac{\partial \mathbf{w}}{\partial \mathbf{u}}$ zero. This is called the *Adjoint* equation

$$\frac{\partial I}{\partial \mathbf{w}}^T + \Psi^T \frac{\partial R}{\partial \mathbf{w}}^T = 0. \tag{10}$$

Thus,

$$\Psi = - \left[\frac{\partial R}{\partial \mathbf{w}} \right]^{-1} \frac{\partial I}{\partial \mathbf{w}}. \tag{11}$$

The expression for the gradient of the cost function then becomes,

$$G = \frac{dI}{d\mathbf{u}} = \frac{\partial I}{\partial \mathbf{u}} - \frac{\partial I}{\partial \mathbf{w}}^T \left[\frac{\partial R}{\partial \mathbf{w}}^T \right]^{-1} \frac{\partial R}{\partial \mathbf{u}}. \tag{12}$$

Virtual Aerodynamic Shaping

We test the flow control algorithms formulated in the previous sections on a *Virtual Aerodynamic Shaping* problem. Here, we take an aerodynamic configuration, and try to make it behave like another aerodynamic configuration under the same free stream conditions by implementing surface flow control.

A basic review of ideal fluid aerodynamics reveals that including a mass source on the surface of an airfoil has the effect of increasing the curvature and including a mass sink has the opposite effect. Given that, for a pre-determined performance measure, every operating condition has an optimum shape, it follows that

a combination of a shape that is optimal for one operating condition, combined with suitably placed sources and sinks will result in a system that meets optimum performance criteria for a wide range of operating conditions.

For the purposes of this study, steady jets are used in order to simplify numerical modeling. Mass flows are prescribed at the wall, and the jets are modeled so as to satisfy the normal velocity/flux conditions at the wall. In addition, the nett. mass flow through the wall is assumed to be zero.

$$\int_{\mathcal{B}_\xi} \rho q_n d\mathcal{B}_\xi = 0. \tag{13}$$

Feedback Nature of Adjoint Based Control

The *Feedback* nature of the *Adjoint* based control laws thus derived become clear, when the *Adjoint* boundary conditions are examined.

The Adjoint Boundary Conditions for Virtual Aerodynamic Shaping

We postulate that the behavior of any aerodynamic configuration, at any freestream condition, is defined by its surface pressure distribution $P_d(\xi, \eta)$. Thus, when we talk about *virtually* shaping one configuration to behave like another, what we really mean to do is to places mass sources and sinks at suitable locations on the configuration such that the resulting pressure distribution $P(\xi, \eta)$ is the same as the target pressure distribution.

To achieve this, we try to minimize a cost function of the form

$$I = \frac{1}{2} \int_{\mathcal{B}_\xi} (P - P_d)^2 d\mathcal{B}_\xi, \tag{14}$$

where P is the pressure at the surface with no controls, and P_d is the desired target pressure. Observe that this cost function is a special instance of the more generic cost function described in Equation (5). We can choose our computational co-ordinates such that $\psi_1 = \psi_3 = 0$, and the normal direction is along ψ_2. When the blowing velocities prescribed at the wall are very small, the *Adjoint* boundary condition reduces to

$$\frac{\partial \mathcal{M}}{\partial P} = \psi^T \frac{\partial F_2}{\partial P} \text{ , on } \mathcal{B}_\xi . \tag{15}$$

For *Virtual Aerodynamic Shaping*, this is simply

$$(P - P_d) = \psi_2 S_{21} + \psi_3 S_{22} + \psi_4 S_{23}. \tag{16}$$

The corresponding *Adjoint* gradient can then finally be expressed implicitly by the equation

$$\delta I = -\int_{\mathcal{B}_\xi} \left(\psi_1 + \psi_2 u + \psi_3 v + \psi_4 w + \psi_5 \left(E + \frac{P}{\rho} \right) \right) \delta \rho q_n d\mathcal{B}_\xi . \tag{17}$$

It can be seen from Equation (16) that the *Adjoint* boundary condition is dependent on the difference between the desired state of the system P_d and the current state of the system P. Moreover, Equation (17) clearly shows that the *Adjoint* Gradient depends only on the flow variables at the boundaries. Thus, it is clear that the *Adjoint* based control thus derived is *Feedback* based.

It should be noted however, that the *Adjoint* equation is solved using the computed state of the flow field and not the measured state. This bypasses the need for global measurements of the flow-field.

Results

2-D results

An RAE-82 airfoil was optimized for minimum drag at a Mach number of 0.77. The airfoil was constrained to operate at a C_L of 0.6. The pressure distribution of the optimized section was used as the target distribution for the flow control case, where blowing and suction is used to mimic the shape changes that lead to the desired pressure changes. The flow calculations were done on a 192×32 grid.

The original (solid) and optimized (dotted) airfoil are shown in Figure 19. The blowing and suction
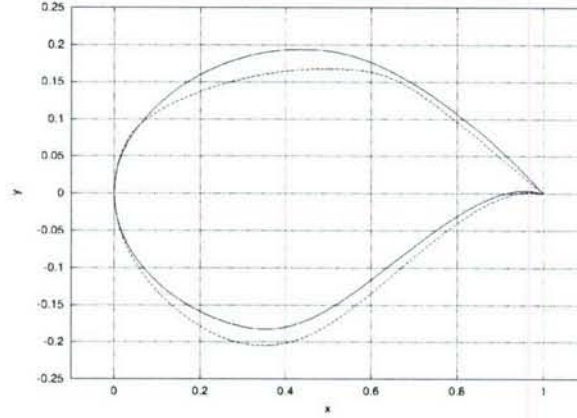
Figure 19: RAE-82 optimized for minimum drag at Mach 0.77: Original (solid) and Optimized (dotted)

velocities that produce the same pressure distribution are shown in Figure 20. As expected, the controller implements blowing on the lower surface and suction on the upper surface. This corresponds very well with the shape change being represented, where the curvature is increased on the lower surface and decreased on the upper surface.
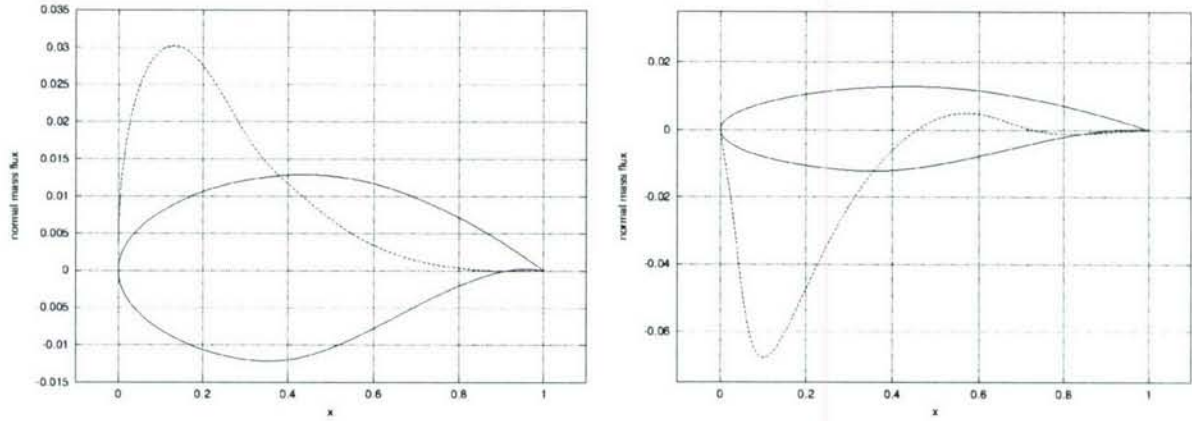

Figure 20: RAE-82: Flow control velocities on the lower (left) and upper (right) surfaces for *Virtual Aerodynamic Shaping*

The Pressure distributions before and after applying flow control are shown in Figure 21. It can be seen that the flow control algorithm derived for the *virtual* aerodynamic design case achieves the desired results.
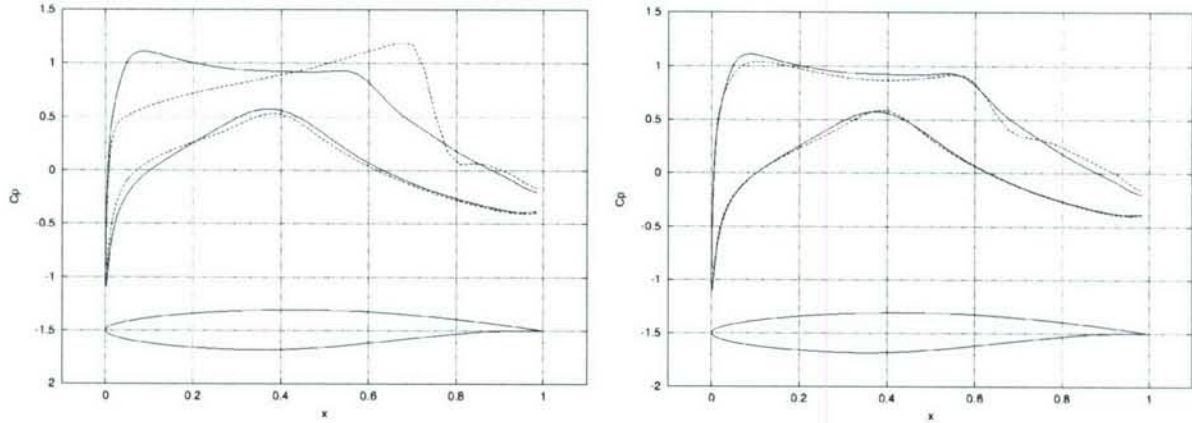
Figure 21: Pressure distributions: target (solid) and actual (dotted) before (left) and after (right) flow control

Reduction in the number of actuators: Design Trade-off

The results included in the previous section were for the case where blowing and suction is implemented continuously along the surface of the airfoil. Implementing this is not practical. We therefore try to reduce the number of actuators.

We would prefer to automatically arrive at the optimum number of actuators needed, and their locations. We do this by looking at the *Adjoint* gradient. The *Adjoint* gradient represents the sensitivity of the cost function with respect to the control variables. The numerical values of the gradient derived thus indicate which controller locations are most effective and which controller locations are least effective.

In order to frame this mathematically, we chose to include all locations where the control input required was atleast 70 percent of that where the effort was maximum, and set the blowing/suction velocities at all other locations to zero.

$$\text{if } \rho q_n(\xi) \leq 0.7 \max \rho q_n \,, \quad \rho q_n(\xi) = 0. \tag{18}$$

It can be seen from Figures 22 and 22 that, suction control is applied only between about 5 percent chord and 30 percent chord on the upper surface, and no control is applied otherwise. The magnitude of suction required is about the same as that in the continuous control case (20).

Design Trade-off: The results of this experiment can be seen in Figure 23. It can be seen that the desired pressure distribution is almost obtained. The match between the desired and actual pressure distributions are quite close especially at the leading edge where the control is applied. In general, we make a compromise when we move from infinite dimensional control to finite dimensional control. The trade-off between the level of control accuracy desired and the number/location/size of the controllers that can be implemented is a design choice. The current section merely presents the algorithm that one would use to study the ramifications of such a tradeoff.

3-D Results

Finally, we check to see if we can achieve similar results in 3 dimensions. The Surface Pressure distribution of an ONERA M6 wing, constrained to operate at a C_L of 0.3 and a Mach number of 0.84 is shown in Figure 24. We try to achieve the same surface pressure distribution at the same freestream conditions for another wing that has a NACA 0012 section. The flow calculations are performed on a $192 \times 32 \times 48$ grid. It can be seen from Figure 24 that, after 5 control iterations, the surface pressure distribution resembles that of
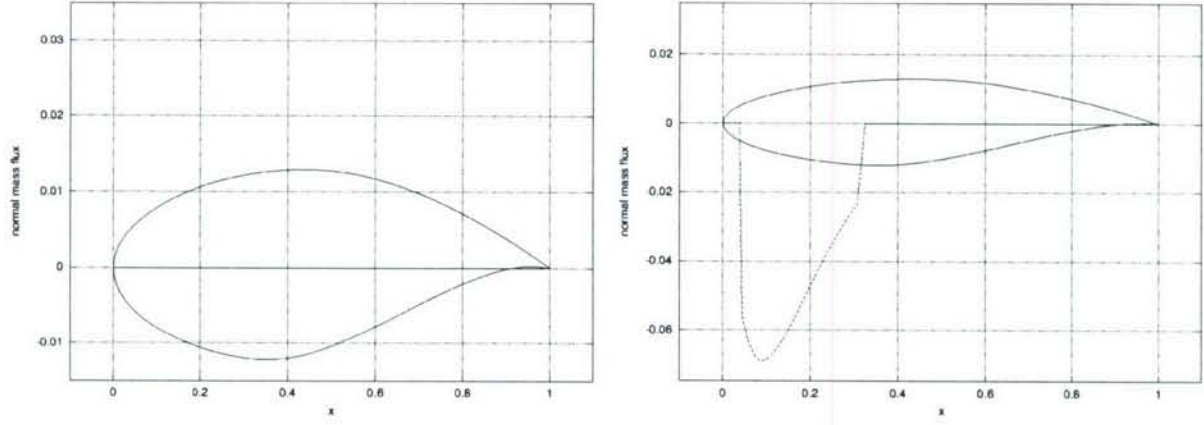
Figure 22: RAE-82: Flow control velocities on the lower (left) and upper (right) surface for *Virtual Aerodynamic Shaping* – reduced number of actuators
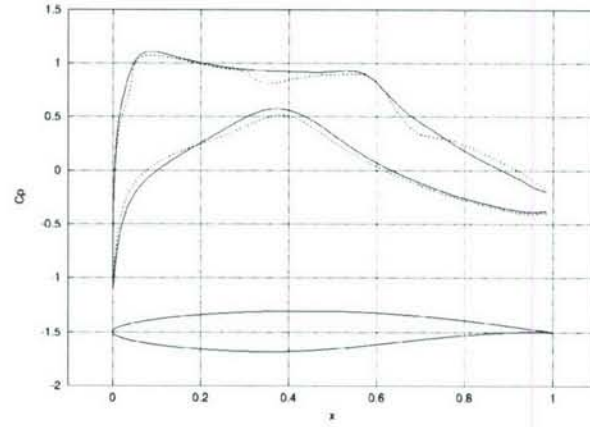

Figure 23: Pressure distributions: target (solid) and actual (dotted) after flow control - Reduced number of Actuators

the ONERA M6. The pressure distributions along the front portions of the wing are almost identical. The pressure distributions along the trailing edge exhibit a slight difference. The original pressure distribution on the NACA 0012 wing is shown in the dotted lines.
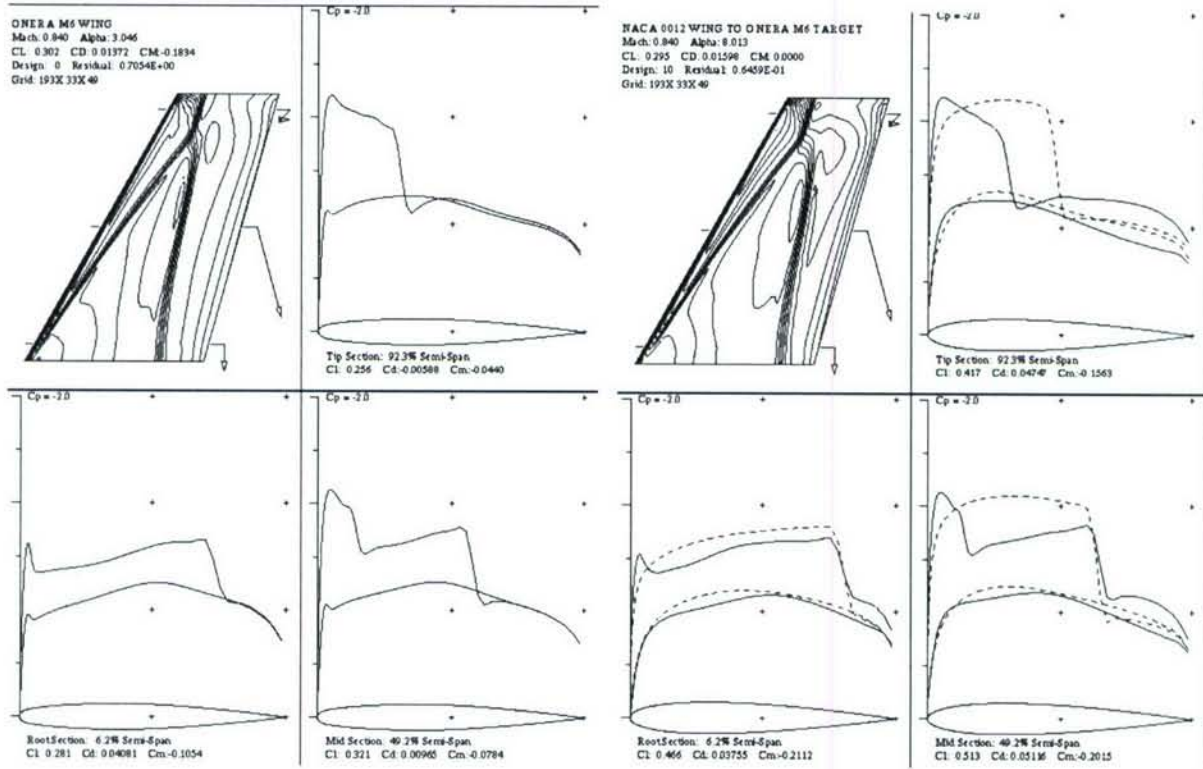

Figure 24: Cp distribution over the surface of an Onera M6 wing at $M = 0.84$ and $C_L = 0.3$ (left) and *Virtual Aerodynamic Shaping* of a NACA 0012 wing to match the surface pressure distribution of an Onera M6 wing at $M = 0.84$ and $C_L = 0.3$ (right)

An Algorithmic Approach to Flutter Control

The structural design of an airplane is guided by static and dynamic factors. The more stringent constraints on the structural design are due to dynamic loads, caused by aero-elastic interactions. One of the most commonly encountered problems in aeroelasticity is flutter [1], a term that is used to recognize the transfer of energy from unsteady aerodynamics associated with the surrounding fluid to the wing structure, resulting in rapidly divergent behavior. If flutter can be controlled at cruise speeds, we can design lighter wings and consequently more efficient airplanes. It is therefore, in the aircraft designer's best interest to design innovative ways in which flutter can be controlled without making the resulting structure too heavy.

0.1 8

2-D Flutter Control In the present section we will investigate the aeroelastic behavior and control of a 2-D airfoil whose schematics is shown in Figure 25. A 2-D airfoil model can be shown to be a fair representation for flutter prediction as shown by Theodorson and Garrik [3] of a straight wing of a large span by giving it the geometric and inertial properties of the cross-section three quarters of the way from the centerline to the

29

wing tip. The equations of motion of this simple system can be shown to be as follows.
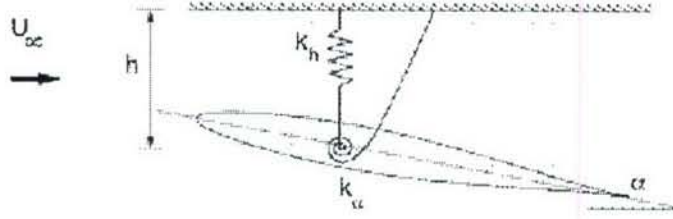

Figure 25: Typical Section Wing Model Geometry

$$m\ddot{h} + S_\alpha \ddot{\alpha} + K_h h \;\;=\;\; -L \tag{19}$$
$$S_\alpha \ddot{h} + I_\alpha \ddot{\alpha} + K_\alpha \alpha \;\;=\;\; M_{ea} \tag{20}$$

K_h and K_α are representative of the bending and torsional stiffness of the wing about its elastic axis.

The elastic axis is the locus of points about which, if a force is applied, doesn't result in any rotation about that point. m and I_α are the mass and moment of inertia of the wing section about the elastic axis. S_α is the coupling term which depends on the relative position of the center of gravity and the elastic axis.

We assume that the structural properties are fixed and we have some amount of control of the right hand sides of Equations (19) and (20) via blowing and suction. The objective is to find a suitable control law which will modify the aerodynamic terms so as to prevent flutter.

Computational simulation

The flow is simulated by solving the unsteady *Euler* equations. The *Euler* equations are solved using a dual time stepping method, using a third order backward difference formula in time, and a symmetric Gauss Seidel scheme for solving the inner iterations. The above mentioned flow simulation code is integrated with a two degree of freedom structural model given by Equations (19) and (20). The coupled aero-structural system is integrated using the *Newmark* scheme. The simulation techniques are discussed in detail in Chapter 2 and Appendix B of the thesis of Palaniappan's.

System Linearization and Model Order Reduction

In Equations (19) and (20), the structural parameters are constant. The lift L and the moment M are complex nonlinear functions of the system state $\mathbf{w}$, α, $\dot{\alpha}$, h and $\dot{h}$. Moreover, α, $\dot{\alpha}$, h and $\dot{h}$ are itself functions of the system state $\mathbf{w}$. Here the state $\mathbf{w}$ is the vector consisting of all the *Euler* states at all finite volumes used in the simulation. Thus

$$L \;\;=\;\; L(\mathbf{w}, \mathbf{u}) , \tag{21}$$
$$M \;\;=\;\; M(\mathbf{w}, \mathbf{u}) . \tag{22}$$

Linearizing about the nominal operating point, we get

$$L \;\;=\;\; \frac{\partial L}{\partial \mathbf{w}}^T \delta\mathbf{w} + \frac{\partial L}{\partial \mathbf{u}}^T \delta\mathbf{u}, \tag{23}$$

$$M \;\;=\;\; \frac{\partial M}{\partial \mathbf{w}}^T \delta\mathbf{w} + \frac{\partial M}{\partial \mathbf{u}}^T \delta\mathbf{u}. \tag{24}$$

It should be noted that for a simulation with one million finite volumes, the dimension of $\mathbf{w}$ is four million for a 2-D simulation and five million for a 3-D simulation. Thus evaluating the above derivatives is a formidable

30

computational challenge. It is also important to recognize that not all the derivatives are significant in the above representation. Consider, for example, a cell in the far-field. The value of the state variables there is not going to change by much, however rapid the oscillations. Therefore, it is of very little use evaluating these derivatives in our linearized model.

Instead, we choose to obtain a suitable reduced order model that captures the essential physics. The most obvious reduction that we can obtain is in terms of α, $\dot{\alpha}$, h and $\dot{h}$. We therefore work with a model of the form:

$$L = L_\alpha \alpha + L_{\dot{\alpha}} \dot{\alpha} + L_h h + L_{\dot{h}} \dot{h} + \frac{\partial L}{\partial \mathbf{u}}^T \mathbf{u}, \tag{25}$$

$$M = M_\alpha \alpha + M_{\dot{\alpha}} \dot{\alpha} + M_h h + M_{\dot{h}} \dot{h} + \frac{\partial M}{\partial \mathbf{u}}^T \mathbf{u}. \tag{26}$$

Equations (25) and (26) assume that the nominal values of α, $\dot{\alpha}$, h and $\dot{h}$ and $\mathbf{u}$ are zero, respectively. Thus for the flutter control problem being studied, the following state vector is used:

$$\mathbf{x} = [\alpha \quad \dot{\alpha} \quad h \quad \dot{h}]^T \tag{27}$$

System Identification: Evaluation of Sensitivities

In our aero-strucutral model (19) and (20), the lift L and the moment M depend on the complete system state $\mathbf{w}$. However, using a full order state model to design a controller is not feasible, given the extremely high dimensionality of the system. We therefore, formulate a reduced order model of the system as shown in Equations (25) and (26). In order for this model to be complete, we need to evaluate the sensitivities with respect to the reduced order state $\mathbf{x}$ and the control variables $\mathbf{u}$.

Sensitivities with respect to the state variables

The sensitivities of the lift and moment with respect to the state variables are evaluated in two different ways.

Theodorsen theory: First, we use theoretical results from Theodorsen [1]. Theodorsen theory assumes that the airfoil under consideration is thin, and is oscillating in an incompressible flow. Under these considerations

$$L_\alpha = \pi \rho v_\infty^2 c \quad , \quad L_{\dot{\alpha}} = \frac{\pi \rho v_\infty c^2}{4},$$
$$L_h = 0 \quad , \quad L_{\dot{h}} = \pi \rho v_\infty c,$$
$$M_\alpha = \frac{\pi \rho v_\infty^2 c^2}{4} \quad , \quad M_{\dot{\alpha}} = 0,$$
$$M_h = 0 \quad , \quad M_{\dot{h}} = \frac{\pi \rho v_\infty c^2}{4},$$

Here ρ is the freestream density, v_∞ is the freestream velocity and c is the chord of the airfoil.

Least-Squares Method: In the second method, we evaluate the sensitivities, by studying the unforced response of a pitching airfoil, and then estimating the sensitivities by a least-squares technique. The aero-structural response of the system over a period of time is similar to the unforced response reproduced in

31

Figures 27, 27, 28 and 28. These simulations provide numerical values for

$$\begin{aligned} \alpha &= f_1(t) \\ \dot{\alpha} &= f_1'(t) \\ h &= f_2(t) \\ \dot{h} &= f_2'(t) \\ L &= f_3(t) \\ M &= f_4(t) \end{aligned}$$

We now try to fit the data thus obtained to functions of the form

$$\begin{aligned} L &= L_\alpha \alpha + L_{\dot{\alpha}} \dot{\alpha} + L_h h + L_{\dot{h}} \dot{h}, \\ M &= M_\alpha \alpha + M_{\dot{\alpha}} \dot{\alpha} + M_h h + M_{\dot{h}} \dot{h}. \end{aligned}$$

Our goal is to evaluate the sensitivities L_α, $L_{\dot{\alpha}}$, L_h, $L_{\dot{h}}$, M_α, $M_{\dot{\alpha}}$, M_h and $M_{\dot{h}}$. We do this using a least-squares technique.

It can be seen from the simulation results that both techniques work quite well The system identification by the least-squares technique, works slightly better, in the sense, it achieves faster stabilization. This can be attributed to the fact that this represents the nonlinear system more closely.

Sensitivities with respect to the control variables

We also need to evaluate the sensitivities of L and M with respect to the blowing and suction velocities $\mathbf{u}$, $\frac{\partial L}{\partial \mathbf{u}}$ and $\frac{\partial M}{\partial \mathbf{u}}$ respectively.

We do this are using an *Adjoint* method as outlined in Chapter .

Flutter Control: Formulation of the Objective Function

We can define the flutter velocity as that point where we have sustained oscillations of the system. Let us define the state vector $\mathbf{x}$ as follows

$$\mathbf{x} = [\alpha \quad \dot{\alpha} \quad h \quad \dot{h}]^{\mathbf{T}} \tag{28}$$

The control vector $\mathbf{u}$ is the vector of blowing/suction velocities at the wall. The dynamics of the system is represented by (19) and (20). For the purposes of designing a controller, we model the lift L and the moment M using a reduced order model as presented in Equations (25) and (26). The system model used to design a controller is then

$$m\ddot{h} + S_\alpha \ddot{\alpha} + K_h h = -\left(L_\alpha \alpha + L_{\dot{\alpha}} \dot{\alpha} + L_h h + L_{\dot{h}} \dot{h} + \frac{\partial L}{\partial \mathbf{u}}^T \mathbf{u} \right)$$

$$S_\alpha \ddot{h} + I_\alpha \ddot{\alpha} + K_\alpha \alpha = \left(M_\alpha \alpha + M_{\dot{\alpha}} \dot{\alpha} + M_h h + M_{\dot{h}} \dot{h} + \frac{\partial M}{\partial \mathbf{u}}^T \mathbf{u} \right).$$

This can be re-phrased in state space form as follows:

$$M\dot{\mathbf{x}} = \hat{A}\mathbf{x} + \hat{B}\mathbf{u}. \tag{29}$$

Here the matrix $\hat{B}$ represents the sensitivities of the state vectors with respect to the control variables. This can be obtained by solving the *Adjoint* equations. Inverting M, we get a system of the form

$$\dot{\mathbf{x}} = A\mathbf{x} + \mathbf{B}\mathbf{u}. \tag{30}$$

32

It is possible to design a controller for the system (30) using LQR techniques [2]. The objective of the problem is to control the system given by (30), so that the final value of the state vector is given by

$$\mathbf{x_f} = [\alpha_f \quad 0 \quad h_f \quad 0]^T \tag{31}$$

If this is rephrased as an optimization problem, the objective would be to minimize the following function:

$$J = \frac{1}{2} \int_0^T \left((\mathbf{x} - \mathbf{x_f})^T Q (\mathbf{x} - \mathbf{x_f}) + \mathbf{u}^T R \mathbf{u} \right) dt \tag{32}$$

where Q is a positive semi-definite weighting matrix and R is a positive definite matrix. In our case,

$$
\begin{aligned}
Q &= I, \\
R &= \varepsilon I,
\end{aligned}
$$

where I is the identity matrix, and ε is a small positive constant. R is required to be positive definite, to ensure that the control computed is not of unreasonable magnitudes.

Backsubstitution of the Control Law into the Nonlinear System

A *Feedback* control gain matrix of the stanford LQR form is then derived for the flutter control problem. Now, the aero-structural system is simulated with blowing and suction control applied at the actuator locations. The magnitude of control required at each actuator location is given by the control gain matrix K_{ss}

$$\mathbf{u} = K_{ss}\mathbf{x}. \tag{33}$$

It can be seen that this control law was successful in stabilizing the system. The results are presented in the next section.

Results

The following experiments were conducted on a symmetric NACA 0012 airfoil at a freestream Mach number of 0.3. A 160×32 grid was used for the CFD simulation.

The structural properties were chosen as follows: $I_\alpha = 60$, $M = 60$, $K_h = 60$, $K_\alpha = 60$, and $S_\alpha = 30$. Our nominal rest point is $\alpha = 0°$ and $h = 0$.

Adjoint Gradients

As discussed in the last section, the *Adjoint* method is used to find the gradients of lift and moment with respect to the control variables, namely the blowing and suction velocities on the surface. It should be noted that this is done using a steady flow assumption about the nominal rest point of the system. We used a symmetric NACA 0012 section. So for our case, this nominal rest point was at $\alpha = 0$, and $h = 0$. These gradients are shown in Figure 26.

Application of Feedback Control to the Nonlinear Flutter Problem

The uncontrolled and controlled aero-structural simulations are represented in Figures 27, and 28. It should be noted that even though the *feedback* law is derived from a linearized model of the system, the control is applied to a complete nonlinear model. Two different methods are used to find the aerodynamic derivatives. It can be seen that the least-squares method does a better job than the Theodorsen method for flutter control. This is obvious because this represents the nonlinear system more accurately. The corresponding blowing/suction velocities are shown in Figure 29. It should be noted that the freestream value of ρq_n in our simulation was 1. So the values of blowing and suction controls required is quite small. Moreover, we need zero control input at the equilibrium point, which is what we desire.
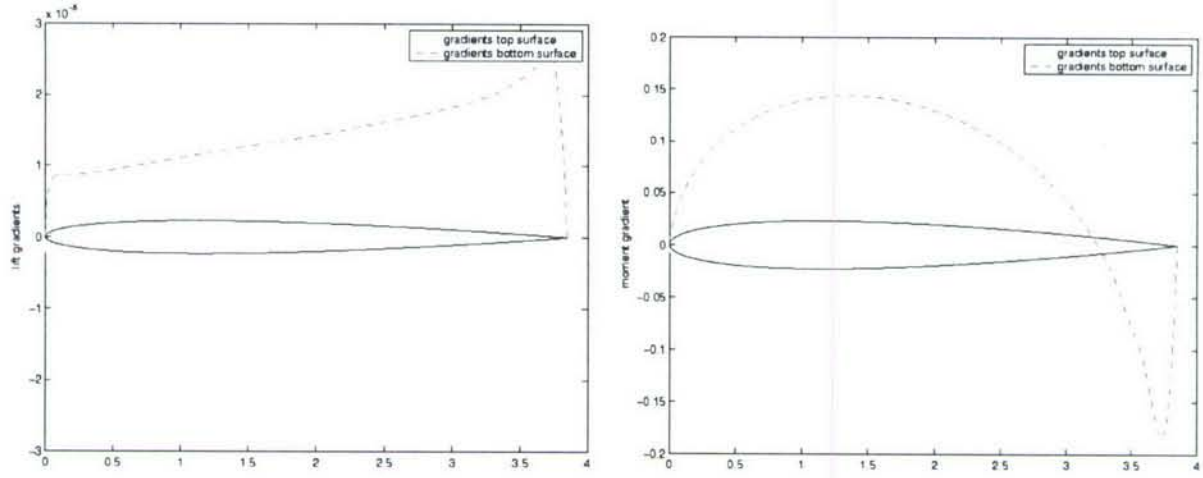
Figure 26: Gradient of lift (left) and moment (right) with respect to control mass fluxes
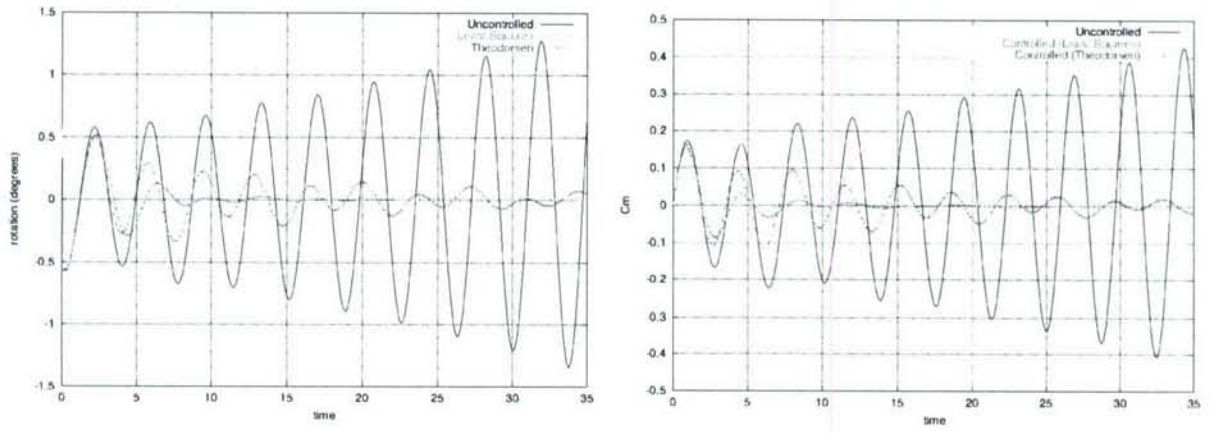

Figure 27: Variation of angle of attack (degrees) with time: controlled and uncontrolled cases (left) and Variation of C_m with time: controlled and uncontrolled cases (right)
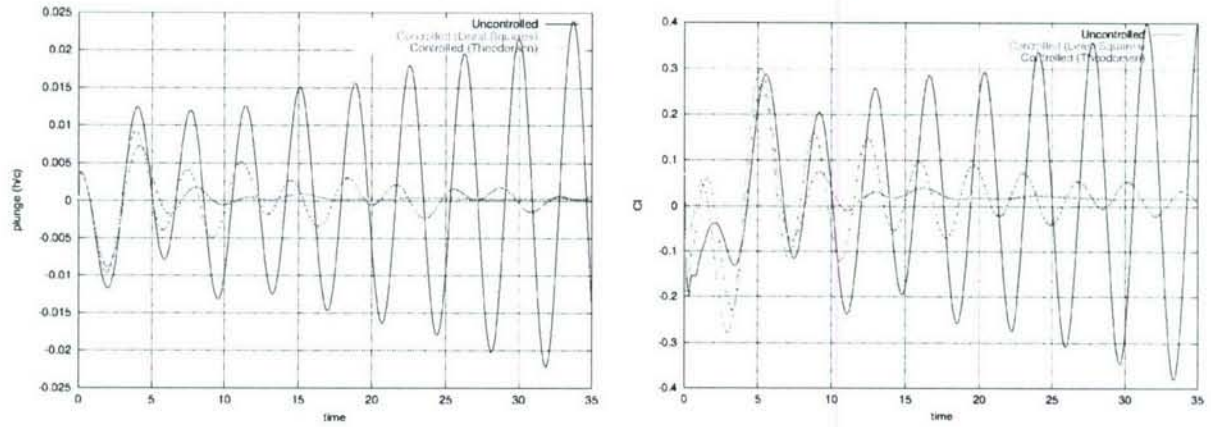

Figure 28: Variation of plunge h/c with time: controlled and uncontrolled cases (left) and Variation of C_l with time: controlled and uncontrolled cases (right)
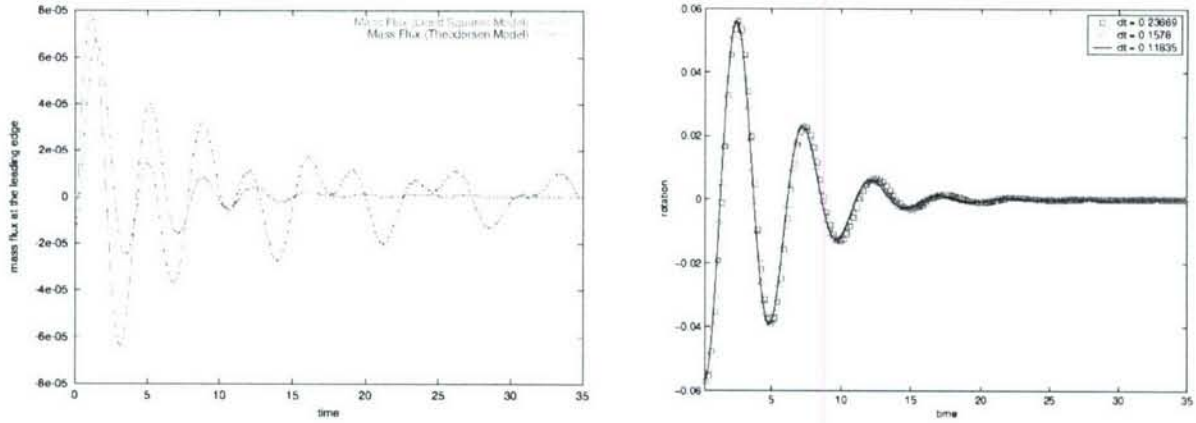
Figure 29: Blowing/Suction mass fluxes at the Leading Edge (left) and Time step refinement studies for the variation of angle of attack with time (right)

Time step refinement studies

To ensure that the flutter control simulations are correct, the time step for the nonlinear aero-structural solver is made smaller and smaller and the controlled behaviour is observed. It can be seen that the pattern of variation of the angle of attack with time is fairly well predicted by the solver. (See Figure 29).

Reduction in the number of Actuators

Our next step is to specialize the control law thus derived to work when the number of actuators is finite. It was found that flutter could be controlled with as few as four actuators: one each in the leading and trailing edges and one each in the middle of the upper and lower surfaces. The fact that there are only four actuation points is represented by zeroing out the gradient shown in Figures 26 and 26 everywhere except at these four locations. (Every location is represented by a small cluster of CFD cells to prevent numerical instability and damping of the actuation values.)

The entire procedure outlined in the previous section is then repeated to derive the *feedback* gain matrix K_{ss}. It can be seen from Figures 30, 30, 31 and 31 that the matrix has non-zero values only at the desired locations of the controllers. Consequently, actuation is performed only at these sites. This is equivalent to controlling the problem with a finite number of actuators.

It can be seen from Figure 32 that flutter is controlled successfully even with a finite number of actuators. This is an important result, as it implies that this system can be implemented on a practical aerodynamic configuration.

3-D Results

We then try to control the flutter of a realistic airplane wing. The wing is unswept and the cross-section is that of a 6 percent thick airfoil obtained by scaling down a NACA 0012 airfoil. The semi-span of the wing is 11.5 inches, and the chord is 4.56 inches. This corresponds to an aspect ratio of about 5.

Structurally, the wing is modeled as a plate of thickness 0.065 inches that is placed along the centerline of the wing-section. The density of the material of the wing is 0.003468 slug/sq. inch. The Young's modulus is 9.848×10^6 slug/sq. inch and the torsional rigidity is 3.639×10^6 slug/sq. inch.
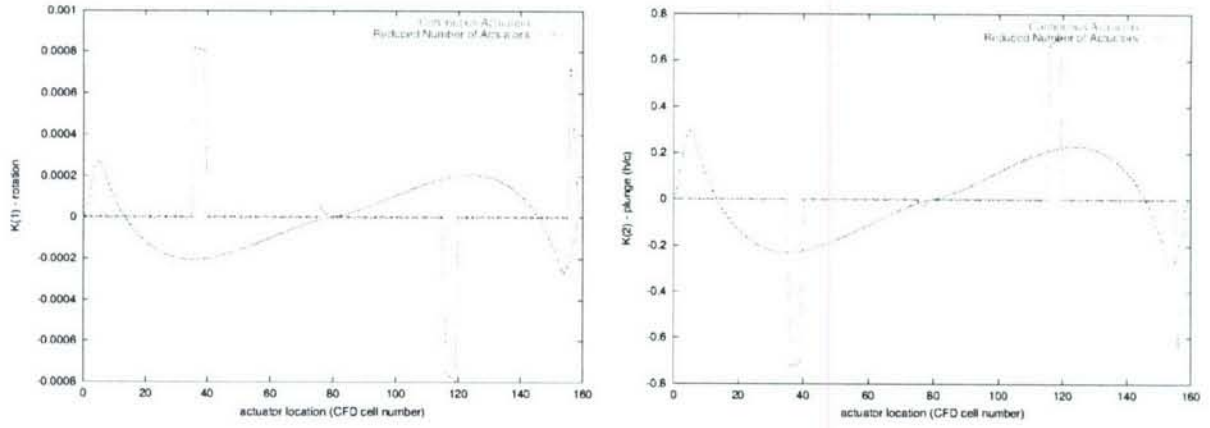
Figure 30: Coefficient of rotation angle vs. actuator number in the feedback gain matrix (left) and Coefficient of plunge vs. actuator number in the feedback gain matrix (right)
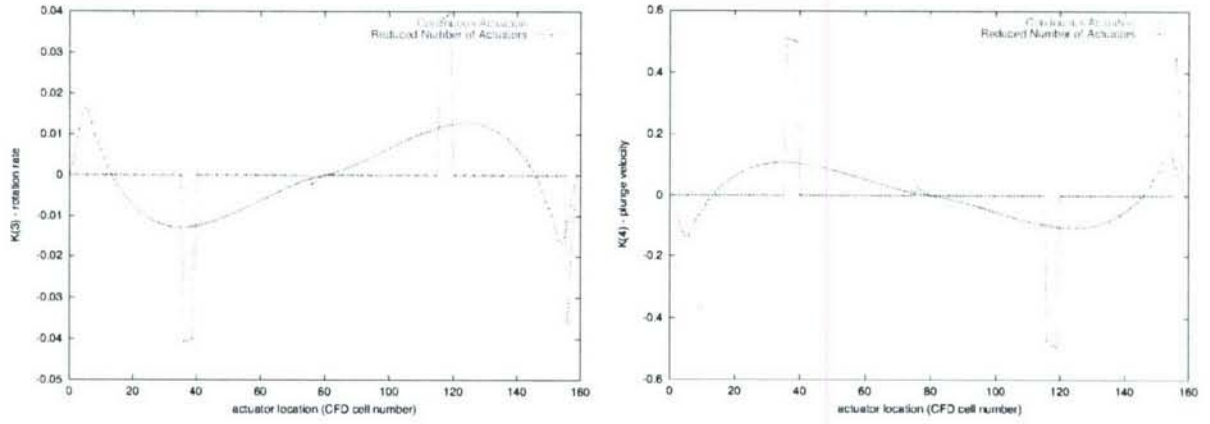

Figure 31: Coefficient of rotation angle rate vs. actuator number in the feedback gain matrix (left) and Coefficient of plunge velocity vs. actuator number in the feedback gain matrix (right)
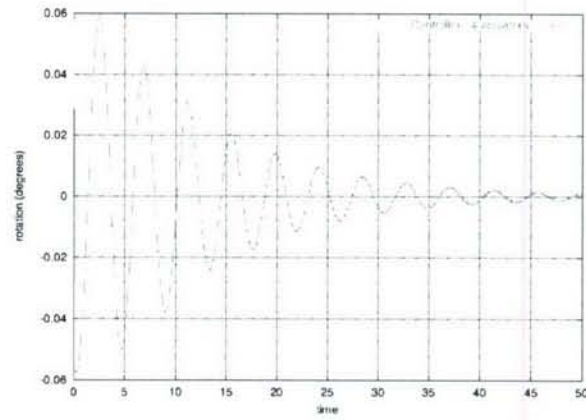

Figure 32: Variation of angle of attack (degrees) with time: with 4 actuators

36

The wing was operated under a freestream Mach number of 0.79 and a freestream dynamic pressure of 5241 Pascal.

The structure is modeled using 50 plate elements. The aerodynamic simulation is done on a $96 \times 32 \times 48$ grid. It can be seen from Figure 33 that the uncontrolled system diverges fairly rapidly. In the time frame considered, the plunge diverges from a negligible amount to 10 percent chord very quickly.

Our task, now, is to design a controller using the techniques described in the previous sections. It has been shown that the flutter of a wing can be studied by studying the dynamics of a section three quarters of the distance from the wing center-line to the tip. We identify the structural properties of the section located at this point, and model it using the typical section wing model, discussed previously. Following the techniques in the previous section, we quickly derive the *feedback* gain matrix K_{ss} for this section.

We make the assumption that this matrix is valid throughout the wing. This is a valid assumption, as the control is implemented in a *feedback* fashion. The tip is expected to go through the maximum deflection, and therefore will be subject to the maximum amount of control. (Since the control is proportional in nature). The root does not move at all, and thus there is no control applied at the root. The results of this simulation are shown in Figure 33. It can be seen that the control law thus derived is successful in controlling flutter. The mass fluxes at an actuator location at the tip, along the trailing edge are shown in Figure 33. Again, it can be seen that the mass fluxes required for control, when compared to the freestream mass flux of $\rho q_n = 1$ are very small.
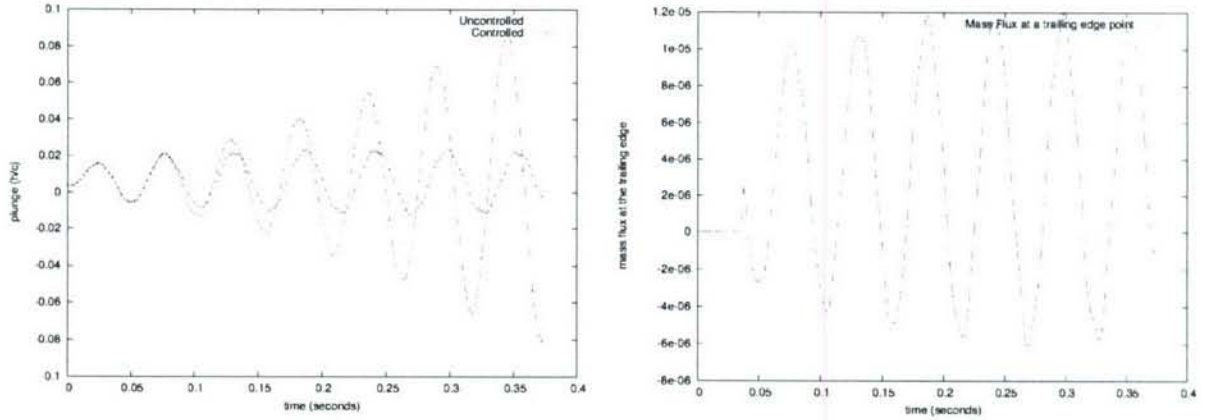

Figure 33: Variation of plunge h/c with time: controlled and uncontrolled cases (left) and Blowing/Suction mass fluxes at a trailing edge point (right)

In the controlled case the wing settles into a limit cycle oscillation of small magnitude as can be seen from Figure 33. This is in spite of the fact that an approximate structural model was used in the calculation of the control law.

This research is described in detail in the thesis of Karthik Palaniappan, entitle "Algorithms for Automatic Feedback Control of Aerodynamic Flows".

References

[1] Raymond L. Bisplinghoff, Holt Ashley and Robert L. Halfman, "Aeroelasticity", Dover Publications, 1996.

[2] A. E. Bryson and Ho Yu-Chi, "Applied Optimal Control: Optimization, Estimation and Control", Taylor and Francis In., 1988.

[3] Theodorsen, T and Garrick, I. E., "Mechanism of Flutter, a Theoretical and Experimental Investigation of the Flutter Problem", N.A.C.A. Report 685, 1940.